Polarization and photon-energy dependent ARPES study on K-doped iron-selenide superconductor

M. Sunagawa[a], K. Terashima[a], T. Hamada[a], H. Fujiwara[a], M. Tanaka[b], H. Takeya[b], Y. Takano[b], M. Arita[c], K. Shimada[c], H. Namatame[c], M. Taniguchi[c], K. Suzuki[d], H. Usui[d], K. Kuroki[d], T. Wakita[a], Y. Muraoka[a], T. Yokoya[a]

[a]*The Graduate School of Natural Science and Technology, Okayama University, Japan*
[b]*National Institute for Material Science, Japan*
[c]*Hiroshima Synchrotron Radiation Center, Hiroshima University, Japan*
[d]*Department of Physics, Osaka University, Japan.*

Keywords: ARPES, iron-based superconductor

Iron-based superconductors are considered to be important for understanding high temperature superconductivity from a new perspective due to the presence of a high superconducting transition temperature (T_c) that cannot be explained within the framework of conventional phonon-mediated BCS superconductivity. In the early days, based on a weak-coupling viewpoint [1,2], the nesting between electron and hole Fermi surfaces (FS) leading to the so-called $s\pm$ state has been considered to be one such key for the emergence of high T_c in iron-based superconductors. However, this theory has faced a serious challenge ever since the discovery of alkali-metal doped iron-selenide superconductors (AFS), where only electron FSs with nodeless superconducting gap have been observed by angle-resolved photoemission spectroscopy (ARPES). [3-5]. The spin fluctuation models based on the weak coupling approach have predicted a *d*-wave superconducting state for systems with only electron-like FSs [6-8], but it is not consistent with the nodeless superconducting gap on the electron-like FS at the Γ point [3-5]. On the other hand, the strong-coupling models based on localized spin picture have predicted a sing-reserved *s*-wave state [9-11], which can explain the nodeless gap structure, but is inconsistent with the observation of the spin resonance mode [12]. Thus, the proposed models based on both the weak- and strong-coupling approaches appear to fail to explain all the experimental results in AFS.

The low-lying electronic structure in iron-based materials consists of multi-band with different orbital character. Due to the photoemission selection rule, the spectral intensity of the bands exhibits photon polarization dependence. Moreover, in several iron-based superconductors, it has been reported that the strength of band intensity also depends on the excitation photon energy. So, there is a possibility that a hole-like FS actually exists and has eluded previous ARPES experiments because of the significant photon polarization and/or photon energy dependence of spectral intensity. In our study, we performed ARPES measurements with careful tuning of photon energy and photon polarization on a high quality single crystal of $K_{0.62}Fe_{1.7}Se_2$ [13], and we succeeded to observe a hole-like band with E_F crossing in two different momentum regions around the Γ point, indicating that a hole-like FS exists in $K_xFe_{2-y}Se_2$. The present study suggests that the alkali-metal doped

iron selenides, with both electron- and hole-like FSs present, can be categorized in the same group as that of the iron arsenides.

REFERENCE

[1] I. I. Mazin *et al*., Phys. Rev. Lett. **101**, 057003 (2008).

[2] K. Kuroki *et al*., Phys. Rev. Lett. **101**, 087004 (2008).

[3] M. Xu *et al*., Phys. Rev. B **85**, 220504 (2012).

[4] D. Mou *et al*., Phys. Rev. Lett. **106**, 107001 (2011).

[5] X. –P. Wang *et al*., Europhys. Lett. **99**, 67001 (2012).

[6] I. I. Mazin, Phys. Rev. B **84**, 02459 (2011).

[7] M. Khodas *et al.*, Phys. Rev. Lett. **108**, 247003 (2012).

[8] A. Kreisel *et al*., Phys. Rev. B **88**, 094522 (2013).

[9] C. Fang *et al.*, Phys. Rev. X **1**, 011009 (2011).

[10] F. Yang *et al*., Phys. Rev. B **88**, 100504 (2013).

[11] R. Yu *et al*., Nat. Commun. **4**, 2783 (2013).

[12] G. Friemel *et al.,* Phys. Rev. B **85**, 140511 (2012).

[13] T. Ozaki *et al*., Europhys. Lett. **98**, 27002 (2012).

Diffraction of the Photoelectron Induced by the Surface Defects/Impurities on the Graphite Surface

Shin-ichiro Tanaka[a]

[a] *Institute of Scientific and Industrial Research, Osaka University, Ibaraki 567-0047, Japan*

Keywords: Graphite, Umklap process, ARPES

Recently, the diffraction of the valence π-band due to the superstructure formed below 30K on the graphite surface was reported by means of the angle-resolved photoelectron spectroscopy (ARPES).[1] The π-band, located at the K-point of the Brillouin zone of the normal graphite, was observed at the Γ-point conserving its dispersion in both the energy and momentum. This is undoubtedly due to the scattering by the $\sqrt{3}\times\sqrt{3}\ R30°$ or larger superstructure which has an inverse lattice vector to connect between the K and Γ points. In the previous work,[1] the superstructure was tentatively attributed to the charge density wave transition at the graphite surface based on the temperature dependent of the photoelectron intensity of the π-band at the Γ-point. However, both of the theoretical [2] and Low-energy electron-diffraction (LEED) [3] studies have shown that the transition of the intrinsic graphite surface is not likely to occur. Therefore, it is highly desired that the origin of the superstructure is examined. It is known that the condition of the sample surface may strongly depend on the procedure of the sample cleaning. A problem of the previous study was that the sample was cleaned only by means of the cleavage of the sample in the vacuum. One of the advantage of the BL-9 in HiSOR is that many ways of the sample treatment including the cleavage, heating etc, are possible *in situ*. In this study, we examine the ARPES spectra of the single-crystal and HOPG graphite after several methods of the cleaning.

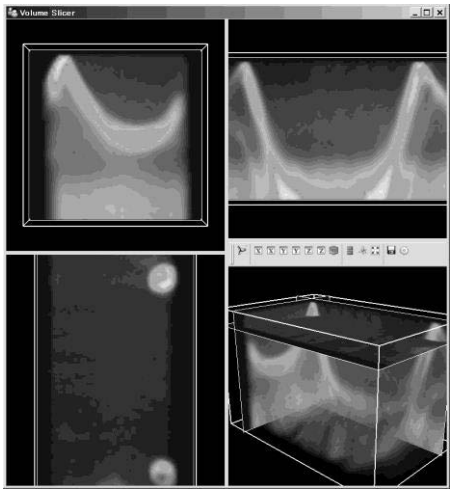

Figure 1: ARPES volume map of graphite

Figure 1 shows the series of the ARPES spectra of the single-crystalline graphite at 12K taken at hν=40eV. The lower-right panel shows the volume map of the photoelectron intensities, where x, y, z axes correspond to the horizontal angle, the vertical angle and the binding energy, respectively, of the photoelectron. The other three panels are projected maps into the two dimensional space of planes in the volume map panel. For making this presentation, the data file was converted into the "vtk" formatted file, and processed with a Mayavi-2 program package, which is popular in the field of the computer graphics. The ARPES spectra show well defined π-band near two K-points of the graphite. According to the previous work,[1] this π-band ought to be observed at the Γ-point below 30K taken at hν=11eV. However, I did not observe the ones in all the samples in variety of the preparation procedures. Instead, rather week π-band near Γ-point was observed but not distinguished at heating at 50K. This result indicate that the superstructure is not an intrinsic nature of the graphite surface but formed stimulated by the defect/impurity, which is often reported by the STM research.[4]

REFERENCES

1. S. Tanaka, M. Matsunami and S. Kimura, Phys. Rev. B 84, 121411(R) (2011)
2. I. Hamada and Y. Morikawa, Phys. Rev. B. 85, 237401 (2012).
3. S. Tanaka and M. Matsumoto, unpublished results.
4. For instance; H.A. Mizes and J. S. Foster, Science, 244, 559 (1989).

Linear-polarization-dependent ARPES measurement of YbB_6

M. Arita[1], H. Sato[1] , K. Shimada[1], H. Namatame[1], M. Taniguchi[1,2], F. Iga[3]
[1]*Hiroshima Synchrotron Radiation Center, Hiroshima University, Kagamiyama , Higashi-Hiroshima 739-0046, Japan*
[2]*Graduate School of Science, Hiroshima University, Kagamiyama , Higashi-Hiroshima 739-0046, Japan*
[3]*College of Science, Ibaraki University, Mito, Ibaraki, 310-8512, Japan*

Rare-earth hexaboride forms CaB_6-type cubic crystal structure. The unusual physical properties appear originated from localized 4*f* bands. It is known that SmB_6 is one of the Kondo insulators and valence fluctuation materials[1]. In theoretical prediction, SmB_6 belongs to topological Kondo insulator in which Dirac-corn-like band structure exists in the *c-f* hybridization gap.

Recently similar hexaboride YbB_6 the attracted researcher's interest as candidate material of topological Kondo insulator. The existence of Dirac-corn-like band structure is predicted in [111] and [110] surfaces in the *c-f* hybridization gap[2]. Although we have measured the electronic structure of YbB_6 by means of ARPES, Dirac corn has not been observed yet.

In this study, we report that electronic band structures near E_F of YbB_6 to clarify the in-gap states. The ARPES measurements have been performed with linear polarized synchrotron radiation at HiSOR BL-9A. We define the S and P polarization geometries as the perpendicular and parallel polarizations respectively, with respect to the incident plane which corresponds to the *xz* plane in Fig 1 (a).

Figures 1 (b) and (c) show the obtained band structure along Γ –X with $h\nu$ = 17.0 eV with S and P geometries, respectively. We found the clear linear polarization dependence around k=0. Although the hole-like band is observed with S geometry, the spectral intensity disappears near E_F with P geometry. It is considered that the hole-like band character on ΓX (XM) high symmetry line has the odd symmetry with respect to ΓXMX plane (*xz* plane). According to the band calculation, the band is mostly derived from B 2*p* character. Therefore the band in ΓXMX plain is attributed to p_y orbital which has node in *xz* plain.

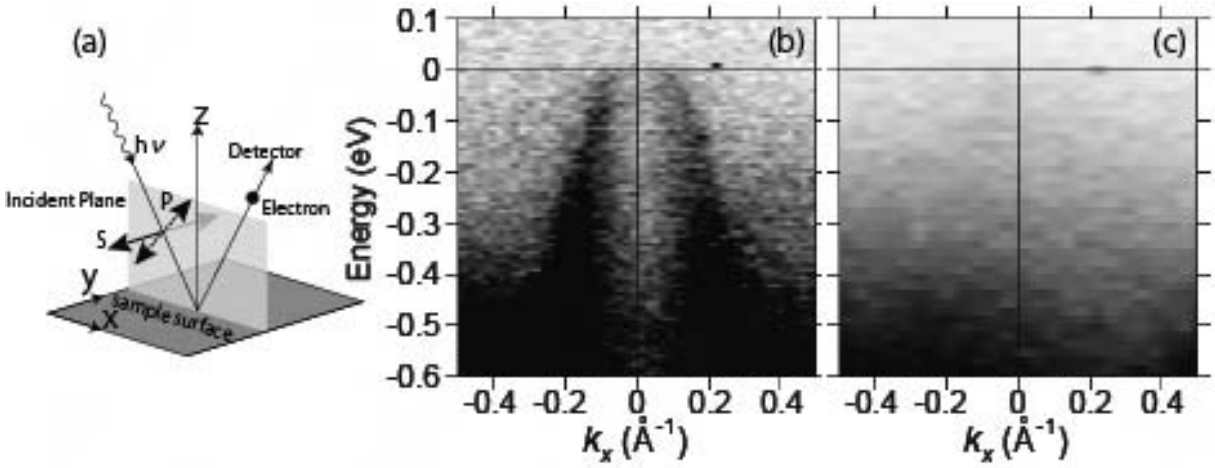

Fig.1 (a) Experimental S and P polarization geometries as the perpendicular and parallel polarizations respectively, with respect to the incident plane. ARPES mapping with (b) S geometry and (c) P geometry in (c).

1) Maxim Dzero et al., Phys. Rev. Lett. 104, 106408 (2010).
2) Hongming Wen et al., Phys. Rev. Lett. 112, 016403(2014).

Angle-Resolved Photoemission Spectroscopy of $Bi_{2.1}Sr_{1.9}Ca(Cu_{1-x}Ni_x)O_{8+\delta}$

W. Mansuer[a], N. Kishimoto[a], H. Takita[a], T. Kubo[a], M. Arita[b], H. Namatame[b], M. Taniguchi[a,b], Y. Kiguchi[c], T. Sakaidani[c], A. Matsuda[c], A. Ino[a]

[a]*Graduate School of Science, Hiroshima University, Higashi-Hiroshima 739-8526, Japan*
[b]*Hiroshima Synchrotron Radiation Center, Hiroshima University, Higashi-Hiroshima 739-8526, Japan*
[c]*Department of Physics, Schools of Advanced Science and Engineering, Waseda University, Okubo 3-4-1, Shinjuku, Tokyo 160-8555, Japan*

Keywords: angle-resolved photoemission, high-T_c cuprates, superconducting gap, element substitution.

Superconducting transition occurs, when electron pairs are formed in solid. The energy for taking an electron apart from the coherent pairs is directly observed as an energy gap by using photoemission spectroscopy. Thus, unusual behavior of the energy gap provides a clue to understanding the mechanism of the high-critical-temperature (high-T_c) superconductivity. The common structure of the high-T_c cuprate superconductors is a two-dimensional CuO_2 plane, where the hybridization of copper $d_{x^2-y^2}$ orbital and oxygen p_x/p_y orbital forms the low-energy electronic band responsible for the superconductivity. Replacing small amount of Cu with another transition-metal element, one can introduce impurities right on the CuO_2 planes, namely the stage of high-T_c superconductivity, and consequently reduce the maximum critical temperature T_c^{max}. This provides us with a good opportunity to investigate the relation between the energy gap and the high-T_c superconductivity.

In this study, we performed high-resolution angle-resolved photoemission spectroscopy (ARPES) of Ni-substituted Bi2212 superconductors, $Bi_{2.1}Sr_{1.9}Ca(Cu_{1-x}Ni_x)_2O_{8+\delta}$ [1]. The ARPES spectra were taken at BL-9A of HiSOR in Hiroshima Synchrotron Radiation Center. Excitation-photon energy and energy resolution were set at $h\nu$ = 8.5 eV and ΔE = 5 meV, respectively. The critical temperatures of the samples of x = 0, 0.01 and 0.03 are T_c = 90, 85 and 70 K, respectively.

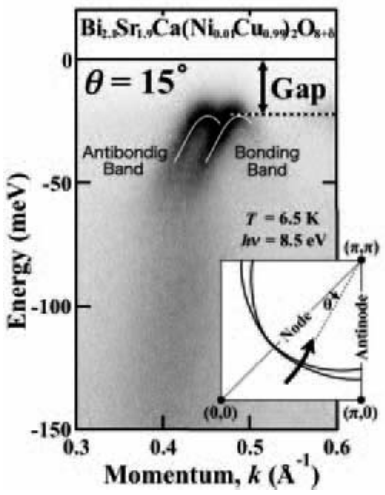

FIGURE 1. ARPES spectra of $Bi_{2.1}Sr_{1.9}Ca(Cu_{0.99}Ni_{0.01})O_{8+\delta}$ (T_c = 85 K), taken along the direction of an off-nodal angle, θ = 15° in a superconducting state at T = 6.5 K. Black regions denote high spectral intensity.

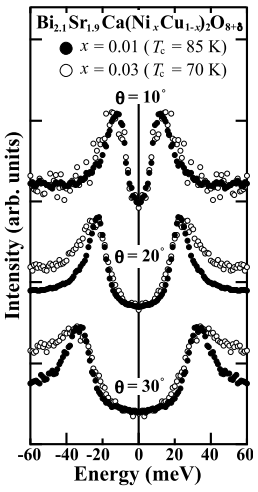

FIGURE 2. Symmetrized energy distribution curves at three off-node angles, θ = 10°, 20° and 30°, for $Bi_{2.1}Sr_{1.9}Ca(Cu_{1-x}Ni_x)_2O_{8+\delta}$. Filled and open circles denote the spectra for x = 0.01 (T_c = 85 K) and x = 0.03 (T_c = 70 K), respectively.

Figure 1 shows the ARPES spectra of 1% Ni-substituted Bi2212 in superconducting state at T = 6.5 K. The measurement path cuts across the Fermi surface at an off-nodal angle of θ = 15°. As shown in Fig. 1, the band dispersion and its splitting are clearly resolved despite Ni substitution. These two branches are assigned to the bonding and anti-bonding bands of the CuO_2 bilayer. The opening of the energy gaps, which are about 22 meV for θ=15°, is also observed for both the bonding and anti-bonding bands. The spectral image in Fig. 1 indicates that the systematic high-resolution gap study is possible for the Ni substituted Bi2212 samples.

Figure 2 shows the energy distribution curves taken at Fermi momenta with typical off-node angles, θ = 10°, 20° and 30° for $Bi_{2.1}Sr_{1.9}Ca(Cu_{1-x}\ Ni_x)O_{8+\delta}$. In order to cancel the effect of Fermi-Dirac distribution function, we symmetrized the spectra following the method explained by Norman *et al*. [2] It seems that the spectral peaks of x = 0.03 are broader than those of x = 0.01, because considerable amount of impurity scattering is introduced by Ni substitution. The notable point is that the energy of the off-nodal superconducting gap hardly decreases, or slightly increases, even though the critical temperature decreases with Ni substitution, x. This implies that the relation between the off-nodal gap and the critical temperature is not straightforward.

In summary, our ARPES study suggests that the energy gap of the bilayer cuprate Bi2212 shows some unusual behavior with increasing the in-plane impurities by substitution of Ni for Cu.

REFERENCES

1. Y. Kiguchi, T. Nakazawa and A. Matsuda, *Phys. Procedia* **58**, 54-57 (2014).
2. M. R. Norman *et al*., *Phys. Rev. B* **57**, 11093-11096 (1998).

Orbital-Selective Spin Characterization of Dirac-Cone Surface State at W(110)

K. Miyamoto[a], H. Wortelen[a], H. Mirhosseini[b], J. Henk[c], T. Okuda[d] and M. Donath[a]

[a] *Physikalisches Institut, Westfälische Wilhelms-Universität Münster, Wilhelm-Klemm-Strasse 10, 48149 Münster, Germany*

[b] *Max-Plank-Institut für Mikrostrukturphysik, Weinberg 2, 06120 Halle, Germany*

[c] *Institut für physik, Martin-Luther-Universität Halle-Wittenberg, Von-Seckendorff-Platz 1, 06120 Halle, Germany*

[d] *Hiroshima Synchrotron Radiation Center, Hiroshima University, 2-313 Kagamiyama, Higashi-Hiroshima 739-0046, Japan*

Keywords: Dirac-cone surface state, spin-orbit interaction, spin-ARPES

Recently, for the topological surface state (TSS) of Bi_2Se_3, several groups have observed an interesting phenomenon by spin- and angle-resolved photoemission (SARPE): the observed spin features of the photoelectrons are strongly dependent on the light polarization [1,2]. This effect is currently highly debated in the field of optospintronics. Although this effect might be dependent on crystal symmetry, so far, the observations of the effect are limited to surfaces with C_{3v} symmetry.

Very recently, we have discovered that the surface of W(110) shows a spin-polarized Dirac-cone state within a spin-orbit-induced gap, which is reminiscent of a TSS [3]. Here, in contrast to so-far studied topological insulators, the surface structure has C_{2v} symmetry. The C_{2v} symmetry strongly influences the dispersion of the Dirac-cone surface state, resulting in a flattened Dirac-cone. Thus, W(110) is suitable to research the spin feature of the photoelectrons dependent on the light polarization on material with C_{2v}.

We studied the orbital dependence of spin feature of the Dirac-cone-like surface state along $\overline{\Gamma H}$ at W(110) by using SARPE with *s*- and p-polarized light as shown in Fig.1. We have noted that the observed spin feature of photoelectron excited by p-polarized light is opposite to the case of s-polarized light. According to dipole selection rule, we can observe the spin feature of even orbital symmetry and odd orbital symmetry by *p*-polarized light and *s*-polarized light, respectively. Therefore, we have concluded that the observed spin textures are reversed between even and odd orbital-symmetry. This finding opens a new way to manipulate the spin polarization of photoelectron in systems with C_{2v} symmetry.

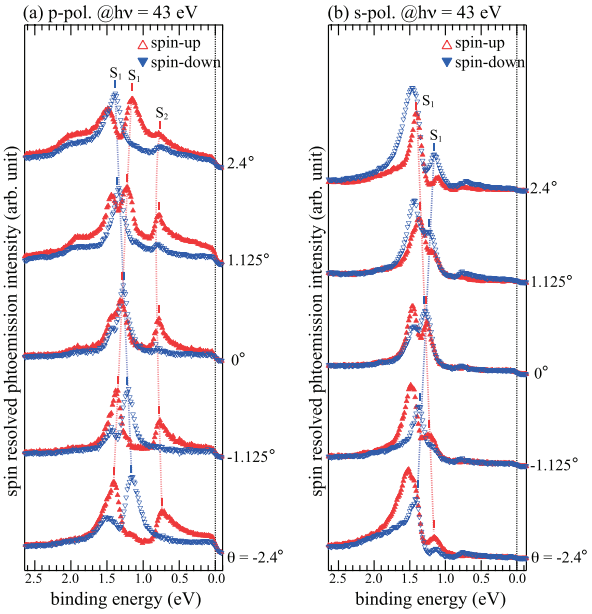

FIGURE 1. Spin-resolved energy distribution curves of W(110) along $\overline{\Gamma H}$ line obtained with *p*-polarized (a) and *s*-polarized light (b) at BL-9B.

REFERENCES

1. C. Jozwiak *et. al.*, Nat., Phys. **9**, 293 (2013).
2. Z. Xie *et. al.*, Nat., Commun. **5**, 3382 (2013).
3. K. Miyamoto *et. al.*, Phys. Rev. Lett. **108**, 066808 (2012).

Proposal No.: 14-A-14 BL-9B

Investigation of Surface Alloy Spin Texture Transfer to Organic Molecular Layer

Jorge Lobo-Checa[a], Patrizia Borghetti[b], Kazuki Sumida[c], Takuya Warashina[c], Taichi Okuda[c] J. Enrique Ortega[a,d,e]

[a] *Centro de Física de Materiales CSIC/UPV-EHU-Materials Physics Center, Manuel Lardizabal 5, E-20018 San Sebastián, Spain*
[b]*Institut des NanoSciences de Paris, Université Paris 6, 4, place Jussieu, 75252 Paris cedex 05, France*
[c] *Hiroshima Synchrotron Radiation Center, Hiroshima University, 2-313 Kagamiyama, Higashi-Hiroshima 739-0046, Japan*
[d]*Departamento Física Aplicada I, Universidad del País Vasco, 20018-San Sebastian, Spain.*
[e]*Donostia International Physics Center (DIPC), Manuel Lardizabal 4, 20018 San Sebastián, Spain.*

Keywords: Organic layers on surface alloys. Spin Orbit Coupling. Spin textures.

The fields of organic electronics and spintronics have the potential to revolutionize the electronics industry. In modern technological devices organic molecules have already become important electronic building blocks due to their low cost, large variability and easy processing. For this reason, organic interfaces have become essential in all emerging electronic applications, including spintronics. Finding suitable substrates that fit the requirements of the desired electronic device is a great challenge. Likewise, the use of molecules to their full capacities requires understanding of the interplay of the molecule-molecule and molecule-substrate interactions. In particular, it is still unknown whether the substrate's spin properties are transferred into the molecular layer or not.

To tackle this problem we studied the well characterized surface alloy $BiAg_2$, with spin textured bands [1], covered with one monolayer of a strong acceptor-like molecule. The chosen molecule is TCNQ-F_4 (Tetrafluorotetracyanoquinodimethane) [2]. The monomers draw the charge from/through the alloyed interface, with the particularity that the electron affinity of TCNQ-F_4 is one of the largest known (up to 3 electrons per molecule) thereby interacting very strongly with the substrate. Unpublished NEXAFS results on this system indicate an important charge transfer into the molecule from the underlying substrate [3], which fills the F-LUMO of the molecule so that the molecular state is shifted to a binding energy of *0.6 eV* (see Fig. 1a). This charge flowing into the molecule leaves the $BiAg_2$ alloy bands unaffected, aside from an overall decrease in ARPES intensity, as previously observed for other molecular systems [4]. This suggests that the charge must flow **through** the $BiAg_2$ and the spin texture of the alloy is unmodified by the organic molecular overlayer.

The open question remaining is whether the electrons flowing through the alloy influence the molecular orbital, such that they gain some spin texture or even become spin split. We have studied this problem by means of SARPES (Spin and Angle Resolved PhotoEmission Spectroscopy) acquiring different energy distribution curves (EDCs) around the 2nd Brillouin Zone (BZ) center (located at $k_{||} = 1.45$ $Å^{-1}$) of the $BiAg_2$ alloy. The reason for choosing the 2nd BZ and not the 1st one is because an intensity node is experimentally found for extended π-orbitals close to normal emission, whereas the intensity peaks away from it [5]. In this way, close to the 2nd BZ we enhance the molecular orbital weight in the spectra while we are still capable of observing the $BiAg_2$ alloy bands.

An example of the obtained SARPES data is shown in panels (c) to (f) of Fig. 1. These spectra have been acquired at $k_{||} = 1.6$ $Å^{-1}$ [red dotted line in panel (a)] using $h\nu = 21.0$ *eV* with linear horizontal polarization and at a sample temperature of *120 K*. The two detector measurable components are shown: the left coincides with the x (in-plane, tangential) direction and the right one is a mixture of z (out-of plane) and y (in-plane, radial) components. For comparison, the signal of the clean $BiAg_2$ alloy is shown at the top panels (c) and (d), whereas the one modified with the molecular overlayer is represented by both bottom graphs (e) and (f) of Fig, 1. In these complex graphs the observed polarization is small, but the spin texture of the alloy before the molecular layer is added is quite clear and follows the reported 1st BZ [1]. When one monolayer of TCNQ-F_4 is added, a state at a binding energy of *0.6 eV* dominates the EDC and appears between the two features corresponding to

each of the $BiAg_2$ spin split branches. The spin polarization is slightly reduced but in no way quenched as we can still observe oscillations which are far larger than the experimental error. This is not only observed at the $BiAg_2$ branches but most importantly at the molecular peak.

In summary, we report a weak spin texture at the molecular LUMO for TCNQ-F_4 even when the spin textured $BiAg_2$ surface alloy does not participate in the charge provided to the molecule. The subtle differences observed in the polarization must be still understood and theoretical support is currently sought. We expect that this work will bring new insight into fundamental processes of organic/solid interfaces, which might be fundamental for the realization of future organic spintronic devices.

We acknowledge financial support from the Spanish Ministry of Economy (MAT2013-46593-C6-4-P), Basque Government (IT621-13) and Hisor.

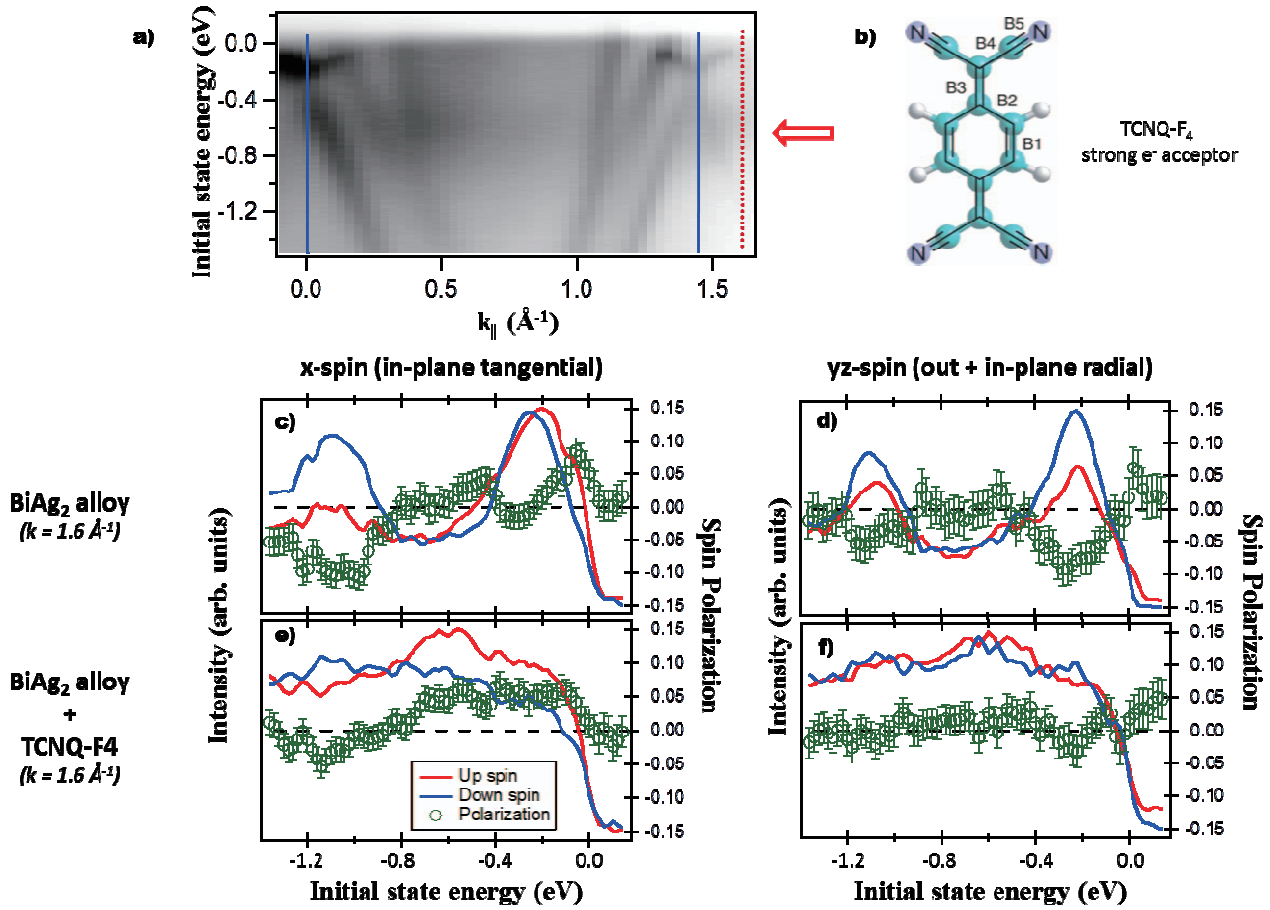

FIGURE 1. Effect of a strong molecular acceptor on the electronic structure of the $BiAg_2$ alloy. (a) ARPES showing the 1st and 2nd Brioullin Zone centers of the $BiAg_2$ alloy after evaporation of 0.5 ML of the TCNQ-F_4 molecule and measured with a He lamp. The non-dispersive feature found around -0.6 eV (indicated with an arrow) corresponds to the electronically filled F-LUMO of the molecule [shown in (b)]. The graphs (c) to (f) correspond to the observed spin texture measured at $k_{||} = 1.6$ Å^{-1} [red dotted line in (a)], where the up spin curve is shown in red, the down spin in blue and the polarization as open green circles. The modification of the initial substrate spin texture (top graphs) after the molecules are deposited on the substrate (bottom panels) can be followed for both detector components (right column x-spin, left column yz spin mixture). In the energy region corresponding to the molecular state a weak spin polarization is observed suggesting a slight transfer of spin from the alloy. These measurements have been acquired at $h\nu = 21.0$ *eV* and *120 K* using linear horizontal polarization.

REFERENCES

1. C. Ast, et al., *Phys. Rev. Lett.* **98**, 186807 (2007); G. Bihlmayer et al., *Phys. Rev. B*, **75**, 195414 (2007).
2. G. M. Rangger, et al., *Phys. Rev. B* **79**, 165306 (2009).
3. D. G. Oteyza and P. Borguetti (private communication).
4. M. C. Cottin, *New Journal of Physics* **16**, 045002 (2014).
5. P. Puschnig et al., *Science* **326**, 702 (2009).

14-A-24 BL-9B

Spin-resolved ARPES of Anomalous Semimetal WTe_2

J. Fujii[a], P. Das[a], I. Vobornik[a], G. Panaccione[a], G. Rossi[a], and M. Kahk[b]

[a]*IOM-CNR Trieste, S.S.14, Km 163.5, AREA Science Park, Basovizza, I-34149, Trieste, Italy*
[b]*Department of Materials, Imperial College London, South Kensington, London SW7 2BP, UK*

Keywords: Spin-resolved ARPES, WTe2, Transition Metal Dichalcogenides.

2D Transition Metal Dichalcogenides (TMD) have attracted significant attention, mainly because their physical properties and chemistry result to be very versatile. Among TMDs, the anomalous bulk properties of semimetallic WTe_2 have been recently highlighted [1]. From the structural point of view, WTe_2 displays an additional structural distortion: the tungsten atoms form zigzag chains along the crystallographic a-axis, producing a quasi 1D arrangement; moreover, WTe_2 is a semimetal (small overlap between valence and conduction bands with no band gap, yet a reduced density of states at the Fermi level) exhibiting an extremely large uniaxial positive magnetoresistance with no saturation [1]. A further parameter to be taken into account is the presence of two heavy elements, pointing to the possible role of spin orbit coupling (SOC) in the relevant energy scale of the system. Here we report angle and spin-resolved photoemission spectroscopy results on WTe_2 single crystals where we are able to disentangle the role of W and Te atoms in the formation of the band structure and identify the interplay of the charge, spin and orbital degrees of freedom.

Spin resolved ARPES spectra are presented in Fig. 1, as measured at hole pocket (panel a, open blue circle), close to Γ on ΓX line (panel b, open red circle) and close to Γ away from ΓX line (panel c, filled green circle). Panel d shows the calculated spin resolved band structure along ΓX . One observes a sizeable spin polarization (P) for an extended binding energy range. It reaches more than 30% for P_y at a binding energy of 0.55 eV (panel a). This fact indicates that there must be not only a broken space inversion symmetry but also a significant influence of SOC in WTe_2. The spin texture is quite complex, with large oscillations in value and sign of P in a narrow energy window, as clearly visible in both Py and Pz (Fig.1a). Such observation is confirmed by the calculation in Fig. 2. The experimental error bar cannot exclude a finite spin polarization also at E_F, yet negligible with respect to values observed at higher binding energies. The Px component is zero along ΓX line (Figs 1(a) and (b)), while we observe non-zero Px component for points away from ΓX (Fig1(c)). This means that the electron spin along ΓX is perpendicular to the W chains, in agreement with calculations that predict only large Py and Pz spin polarizations. Results in Fig 1 a, b (at the hole pocket) and d show the presence of both in plane and out-of-plane component of the spin polarization, in contrast with ordinary Rashba systems where P is only in-plane [2]. The spin polarization changes sign upon crossing the Brillouin zone center, i.e., the sign of P is reversed at K' = -K, as experimentally confirmed in Fig. 1a and 1d , that report the data taken at positive and negative k_x values. This indicates that time reversal symmetry is preserved, i.e. [E(k, σ+) = E(-k, σ-)] and that the observed spin polarization of bands is of nonmagnetic origin. A large spin polarization of electronic bands has been recently reported in the semiconducting TMD WSe_2 where P occurs due to local asymmetry of layers [3]. The consecutive Se-W-Se layers have opposite net dipole moment, which modulate the spin texture strongly even though the global inversion symmetry is preserved. Unlike WSe_2, the crystal structure of WTe_2 is non-centrosymmetric, which opens up the possibility of lifting the spin degeneracy via spin-orbit coupling. The amplitude of spin polarization depends on the strength of SOC, and indicates that SOC forcely must be included in the analysis of WTe_2.

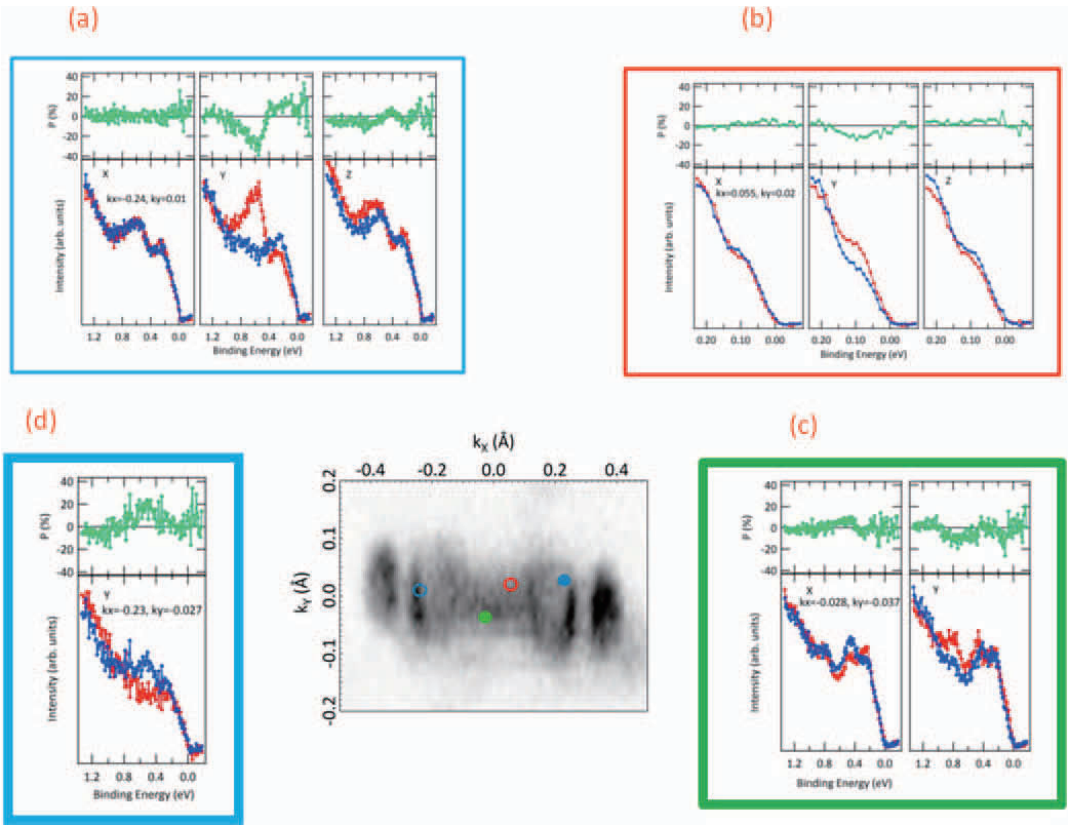

FIGURE 1. Spin resolved ARPES spectra. The measured points in k-space are presented with colored circles on the Fermi surface map.

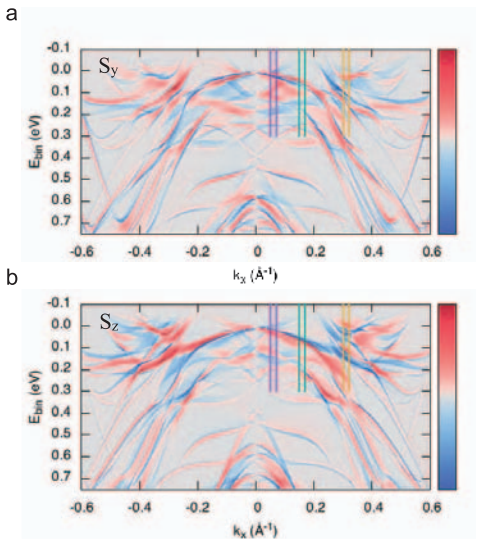

FIGURE 2. Spin resolved band structure along ΓX (calculation) : y component (a) and z component (b).

REFERENCES

1. Ali M. N., Xiong J. et al. Large, non-saturating magnetoresistance in WTe_2, Nature **514**, 205 -208 (2014)
2. Hasan M. Z, Kane C. L., Colloquium: Topological insulators, Rev. Mod. Phys. **82**, 3045 (2010)
3. Riley J. M., Mazzola F., et al. Direct observation of spin-polarized bulk bands in an inversion-symmetric semiconductor, Nature Physics **10**, 835-839 (2014)

Spin and angle resolved photoemission studies on chiral materials

Munisa Nurmamat [a], T. Okuda [a], T. Koyama [b], K. Inoue [b], H. Namatame [a], M. Taniguchi [a,b] and A. Kimura [b]

[a]*Hiroshima Synchrotron Radiation Center, Hiroshima University,2-313 Kagamiyama, Higashi-Hiroshima 739-0046, Japan.*
[b]*Graduate School of Science, Hiroshima University,1-3-1 Kagamiyama, Higashi-Hiroshima 739-8526, Japan.*

Keywords: Chiral materials; Spin polarized angle resolved photoemission spectroscopy.

Chirality is a fascinating phenomenon which can play a crucial role in spintronic devices, where the spin rather than the charge of an electron is used for data transmission and manipulation. In materials science, chiral materials are frequently found in molecules or crystals with helical structures, which break mirror and inversion symmetries but combine rotational and translational symmetries [1]. Unconventional magnetic properties affecting spin transport have been reported for inorganic-inorganic interfaces, topological insulators, graphene, and chiral molecules. Recently, exceptionally high polarization of electrons ejected from surfaces coated with a self-assembled monolayer of double-standard DNA (dsDNA), independent of the polarization of the incident light has been observed [2].

Spin-orbit coupling in hydrocarbons is commonly believed to be very weak, and no appreciable spin alignment is expected. Only a very small preference spin orientation over the other was found, and only when a heavy metal atom with substantial spin-orbit interaction was present in the chiral molecules. For dsDNA which consists of a light element such as carbon atom, it is difficult to present spin-polarized photoelectron by the spin-orbit interaction. So far, the origin of interpreted helical structure of DNA causing the spin-polarized electrons is not clear. Besides, it is difficult to handle DNA in ultra-high vacuum as required for photoelectron spectroscopy. Instead of dsDNA, other chiral materials which are more stable and show strong spin-orbit interaction will be needed.

The chiral helimagnet $Cr_{1/3}NbS_2$ belongs to a large family of layered materials and has attracted a lot of attention as inorganic chiral material. The Cr atoms are intercalated in the octahedral holes between the trigonal prismatic layers of 2H-NbS_2. The intercalation of a transition metal strengthens the bonding with the possibility of charge transfer from the intercalated atoms to the transition metal atoms in the layer, which brings about strong changes in the electronic structure and corresponding changes in the electrical transport and magnetic properties. The chiral magnetic soliton lattice (CSL) has been demonstrated in chiral magnetic crystals of $Cr_{1/3}NbS_2$ by means of Lorenz microscopy and small-angle electron diffraction (SAED) [3]. Furthermore, the magnetic phase transition of $Cr_{1/3}NbS_2$ has been studied by experimentally and theoretically [4]. So far, the spin-polarization of chiral helimagnet $Cr_{1/3}NbS_2$ has not been studied yet.

The samples have been fabricated by the chemical vapor deposition (CVD) method, which usually generate high-quality single crystals. The band structure of chiral material $Cr_{1/3}NbS_2$ and the presence of spin polarization in k-space have been partially performed by using spin and angle-resolved photoemission spectroscopy at the APPLE-II type variable polarization undulator beam line (BL-9B) of Hiroshima Synchrotron Radiation Center (HSRC). Similar to another intercalated transition metal dichalcogenides $Mn_{1/3}NbS_2$ [5], the Fermi surface contours of $Cr_{1/3}NbS_2$ reveals a rounded hexagonal Fermi surface sheet centered at Γ point and a second approximately triangular sheet centered at K point. The spin polarization at K point has been measured by changing the polarization of incident light. Results shows 10% out-of spin component and -10% in-plane spin component with circular polarized light. Further study will be continued. Details of our observations may open new avenues to exploring fascinating functionality and to elaborating a new paradigm for spintronic applications based on chiral materials.

REFERENCES

1. M. Bode et al., Nature **447**,190-193 (2007).
2. B. Göhler et al., Science **331**, 894 (2011).
3. Y. Togawa et al., PRL**108**, 107202(2012).
4. N. J. Ghimire et al., PR**B 87**, 104403 (2013).
5. C. Battaglia et al., Eur. Phys. J. B **57**, 385–390 (2007).

Spin-Orbital Texture of Bi Based Surface Alloys and Sb_2Te_3 Probed by Polarization- and Photon Energy-Dependent SARPES

Seibel, Christoph[a] and Maaß, Henriette[a] and Bentmann, Hendrik[a] and Reinert, Friedrich[a]

[a]*Experimental Physics 7, University of Würzburg, Am Hubland, 97072 Würzburg, Germany*

Keywords: Topological Insulator, Spin-Orbital texture, Rashba-type spin-splitting of surface state.

We performed spin and angle-resolved photoelectron spectroscopy experiments on the topological insulators Bi_2Te_3 and $(BiSb)_2(TeSe)_3$ as well as the giant-Rashba semiconductor BiTeI at varying photon energies ranging from hv = 16 eV up to hv = 28 eV and at low temperatures of approximately T = 80 K. The cleavage of the samples along the (0001)-plane was done by exfoliation at pressures lower than $1*10^{-4}$ Pa, by use of a scotch-tape. The main interest of this beamtime was to determine the complete spin vector, i.e. its radial, tangential and out-of-plane components, of the topological surface states at the Fermi vectors along the different high symmetry directions of the surface Brillouin zone. For this project the ESPRESSO endstation at BL-9B was chosen because of its high energy and angle resolution and measurement efficiency.

The main preliminary result is the detection of a dominant radial spin component of the topological surface state of Bi_2Te_3 for measurements taken along the ΓM direction, using photon energies of hv = 21-22 eV. At first glance this is in contradiction to DFT ground state calculations, in which the spin vector stands perpendicular to the electron wave vector k for both high-symmetry directions. The, at this point still ongoing, analysis consults one-step photoemission calculations. Preliminary theoretical results confirm the experimental observations. By varying the photon energy we additionally focused on occurring matrix elements effects. The result was the observation of a hv-dependent rotation of the detected photoelectron spin vector. Our results indicate a complex deviation of the spin-resolved photoemission signal with respect to the ground state spin vector in Bi_2Te_3.

Our finding for Bi_2Te_3 is supported by measurements of the spin-polarization vector of the Rashba-type surface state at the Te terminated surface of BiTeI. In this case we performed experiments using He I radiation with hv = 21.21 eV. The spin texture of the surface state also showed a finite spin component radial to k, similar to the case of Bi_2Te_3. In the case of BiTeI the probed surface state is of non-topological nature but exhibits the same complex spin-orbital entanglement like the non-trivial surface states in topological insulators. This entanglement is what we assume to give rise to occurring geometry- and photon-energy-dependent results in spin-resolved photoemission measurements.

Spin- and k-dependent electronic structure of Au nanowire on Ni(110)

T. Warashina[a], M. Nurmamat[a, b], K. Miyamoto[b], A. Kimura[a], M. Taniguchi[a, b], H. Namatame[b], and T. Okuda[b]

[a] *Graduate School of Science, Hiroshima University, 1-3-1 Kagamiyama, Higashi-Hiroshima 739-8526, Japan*
[b] *Hiroshima Synchrotron Radiation Center, Hiroshima University, 2-313 Kagamiyama, Higashi-Hiroshima 739-0046, Japan*

Keywords: Spin-ARPES, Rashaba effect

Materials with large spin-orbit interaction (SOI) such as Rashba materials or topological insulators are getting much attention recently because of the possible application for the spintronic devices. The most of these materials posses spin polarized electronic states with two-dimensional character at the surfaces. Modification of the spin-split electronic states by electron confinement in lower dimensionality and/or by the external perturbation (e.g. electric field or magnetic field) is very interesting subject in this field.
It is known that gold atoms form one-dimensional wire structure on Ni(110) surface by self-assembly[1]. The electronic structure of this Au nanowire was investigated by spin- and angle resolved photoemission spectroscopy and the clear one-dimensional character of electronic state was observed[2]. Furthermore the spin analysis reveals that the states have minority spin character and the spin polarization is explained by the spin dependent confinement of the electron on the ferromagnetic surface.

Although it has not been discussed in the previous papers, the large atomic number of Au reminds us the possibility of Rashba spin splitting of the states by the expected large spin-orbit interaction. If this is the case, the system must be very interesting since the effect of low-dimensionality and magnetic field can be investigated.

In this work, as first step, we have evaluated the structure of Au deposited Ni(110) and confirmed well ordered Au nanowire, using scanning tunneling microscopy and low-energy-electron diffraction (LEED), in Fig.1. In this case, Au atoms form dimer-trimer chains oriented along the [001] direction in Ni(110). This result is agreement with the previous work [1].

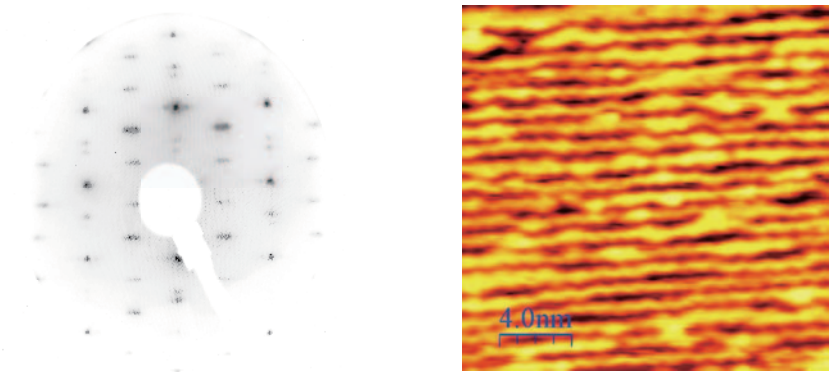

FIGURE 1. LEED pattern (left figure) and STM image (right figure) of 0.7ML Au on Ni(110)

Thereafter, we have investigated the spin electronic structure of Au nanowire by high-resolution spin- and angle-resolved photoemission spectroscopy (spin-ARPES) using ESPRESSO machine at BL-9B in Hiroshima Synchrotron Radiation Center (HiSOR)[3] and have found several Rashba-type spin splitting bands (A and B) formed by Au nanowire as shown in Fig. 2. In particular, the constant energy contour of band A shows flat shapes, which are often observed in one dimensional electronic structure probed by high-resolution ARPES. Finally, we have discovered the Rashba spin-splitting bands in one dimensional system on ferromagnetic substrate. This finding opens a new way to study Rashba effect combined with exchange interaction.

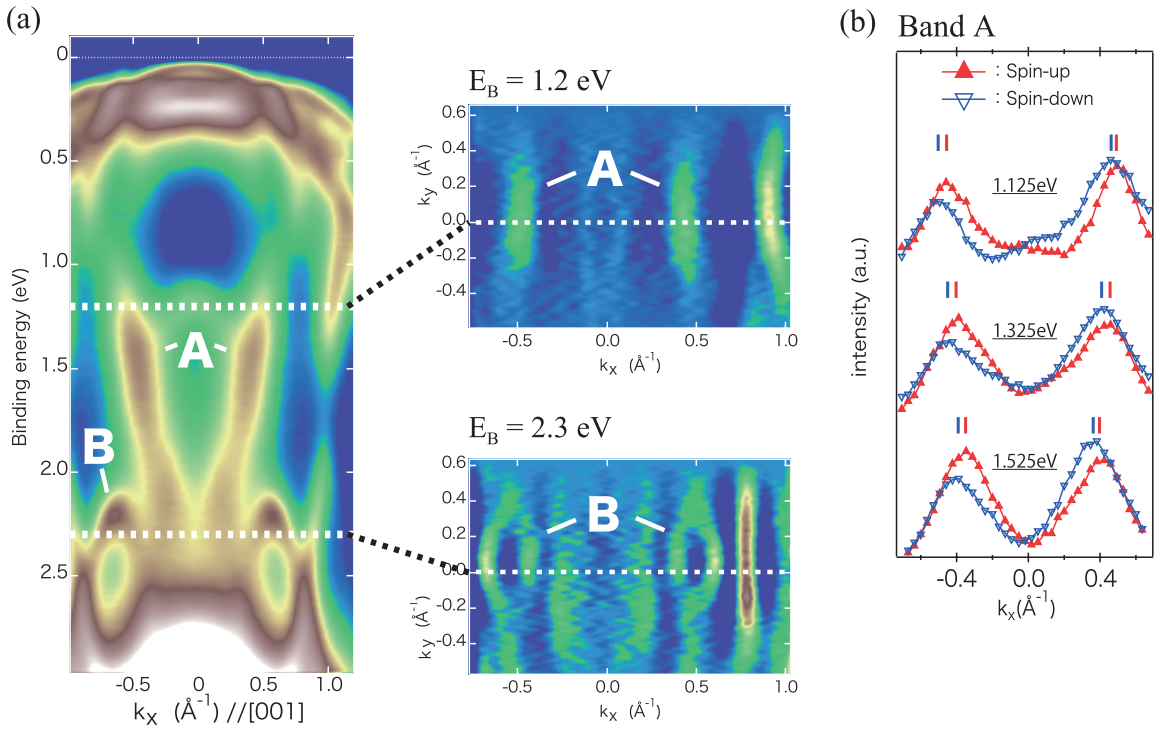

FIGURE 2. (a) energy band dispersion and constant energy contours at E_B=1.2 eV and 2.3 eV in Au nanowire. (b) spin-resolved momentum distribution curves focused on band A as 1.125 eV, 1.325 eV, and 1.525 eV. Red and Blue triangle show the spin-up and spin-down spectra.

REFERENCES

1. L. P. Nielsen, F. Besenbacher, I. Stensgaard, and E. Laegsgaad, Phys. Rev. Lett. 74, 1159 (1995).
2. C. Pampuch, O. Rader, T. Kachel, W. Gudat, C. Carbone, R. Klaesges, G. Bihlmayer, S. Bluegel, and W. Eberhardt, Phys. Rev. Lett. 85, 2561 (2000).
3. T. Okuda, K. Miyamaoto, H. Miyahara, K. Kuroda, A. Kimura, H. Namatame, and M. Taniguchi, Rev. Sci. Instrum. 82, 103302 (2011).

Study of surface spin structure of Bi(110) fabricated on Si(557) surface

T. Okuda[a], T. Shishidou[b], M. Nurmamat[a], E. Schwier[a], H. Namatame[a] and M. Taniguchi[a,c]

[a]*Hiroshima synchrotron radiation center, Hiroshima university*
[b]*Graduate school of Advanced sciences of matter, Hiroshima University*
[c]*Graduate School of Science, Hiroshima University*

Keywords: Rashba effect, Spin-resolved photoemission, first principles calculation

Strong spin-orbit coupling and breaking of space inversion symmetry cause so-called Rashba spin split surface states. Bi is one of the key materials for the emergence of such a spin-split surface states since the spin-orbit interaction is larger in the heavier materials. For instance $BiAg_2$ surface alloy on Ag(111) shows giant Rashba spin-splitting[1] and most of the topological insulators contain Bi atoms. In addition pure Bi crystal itself is also well known that its surface shows strong Rashba spin-split[2]. Especially the Rashba spin-split of Bi(111) surface has been examined precisely both experimentally and theoretically[3]. In case of Bi(111) surface it is reported that one can easily grown the well ordered Bi(111) thin film on Si(111)7x7 clean surface[4]. In application point of view the ability of single crystal fabrication on Si surface is important and one may be able to design the real device by the so-called top-down design methodology in nanotechnology. On the other hand, one may also utilize the bottom-up design methodology like a self-assembling of the surface structure on Si surfaces for controlling the electronic properties. For example one can use vicinal Si surface as the template to fabricate one-dimensional surface states as demonstrated on Au/Si(557), Au/Si(553), and so on[5] and the existence of one-dimensional Rashba spin-split surface states has been established by spin-resolved photoemission[6].

In this study we have attempted to fabricate the anisotropic Rashba spin-split surface states of Bi film using vicinal Si(111), *i.e.* Si(557) surface as the substrate. Our first motivation was to obtain some anisotropic Rashba spin-split states of Bi(111) surface caused by the electron confinement in the

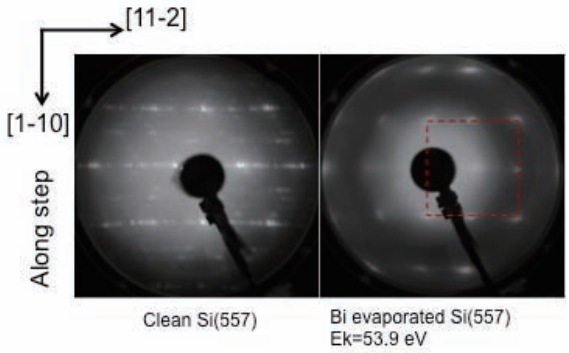

FIGURE 1. LEED pattern of clean Si(557) and Bi film (8 BL) fabricated on Si(557).

narrow terrace of the vicinal Si(111) surface like the anisotropic surface electronic states of Ag film on Si(111)4x1-In[7]. However, the Bi film structure fabricated on the Si(557) surface is not Bi(111) surface but similar to Bi(110) surface as shown in the LEED pattern (See FIGURE 1.). The Fermi surface and band dispersion observed by angle resolved photoemission (ARPES) resemble very much those of Bi(110) single crystal (FIGURE 2.). In order to investigate the spin electronic structure of this Bi(110) like film, we have performed spin-ARPES measurement on the sample and observed clear spin polarization both in-plane and out-of-plane spin components. The observed spin electronic structure is in good agreement with the results of first principles calculation of Bi(110) single crystal indicating that the film has bulk Bi(110) crystal like structure.

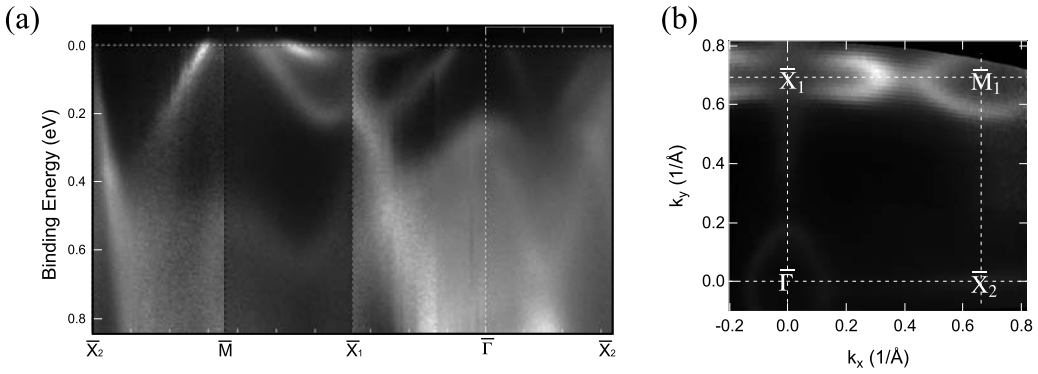

FIGURE 2. ARPES results of Bi film on Si(557) taken with hv=16.0 eV. (a) Band structure and (b) Fermi surface mapping.

REFERENCES

1) C. Ast et al., *Phys. Rev. Lett.* **98**, 186807 (2007).

2) P. Hofmann, *Prog. Surf. Sci.* **81**, 191 (2006).

3) T. Hirahara et al., *Phys. Rev. B* **76**, 153305 (2007).

4) T. Nagao et al., *Phys. Rev. Lett.* **93**, 105501 (2004).

5) J. Crain et al., *Phys. Rev. B* **69**, 125401 (2004).

6) T. Okuda, et al., *Phys. Rev. B* **82**, 161410 (2010).

7) N. Nagamura et al., *Phys. Rev. Lett.* **96**, 256801 (2006).

Changes in electronic states of $Pd_{1-x}M_x$ (M= Ru, Rh, Ag) alloys after hydrogenation studied by X-ray absorption spectroscopy

K. Fujii[a], N. Ishimatsu[a], S. Hayakawa[b], H. Maruyama[a]

[a]*Graduate School of Science , Hiroshima University, Higashihiroshima 739-8526, Japan*
[b]*Graduate School of Engineering, Hiroshima University, Higashihiroshima 739-8527, Japan*

Keywords: X-ray absorption spectroscopy, Hydride, Pd-based alloys, Electronic structure

Hydrogenation of Pd metal occurs even at lower pressures than ambient pressure [1,2]. This property of Pd is of great interest, because other 4*d* metals with more than half filled *d* shells, e.g. Ru, Rh, require the hydrogen pressure P_{H2} above 1 GPa for the hydrogenation. The excellent property of Pd metal for hydrogenation is modified by alloying with small amount of Rh or Ag metal. In the case of Pd-Rh alloys, P_{H2} rapidly raises with increasing Rh content, whereas hydrogen content x in the hydride phase increases slightly [1]. In the case of Pd-Ag alloys, P_{H2} decreases with increasing Ag contents up to the composition $Pd_{0.76}Ag_{0.24}$ accompanied with the rapid decrease in hydrogen content x [2].

Alloying Pd with the neighboring Rh or Ag metal is regarded as a procedure to change the average number of 4*d* electrons in the alloy. However, the different behaviors between P_{H2} and x as a function of Rh or Ag content demonstrate that the hydrogenation properties are not simply interpreted as effects of the changes in the average number of 4*d* electrons. It seems that the hydrogenation properties are influenced by the intrinsic hydrogen absorbing property of each *M* atom; however, it is not fully understood how Rh and Ag atoms participate the hydrogenation of the Pd-*M* alloys. In this study, we have investigated the 4*d* electronic states of Pd-*M* alloys (*M* = Ru, Rh, and Ag) before and after hydrogenation by using x-ray absorption spectroscopy (XAS) at the $L_{2,3}$-edges.

Pd-*M* (*M*=Ru, Rh, Ag) polycrystalline alloys were synthesized by arc melting method. The ingot was cut by a low speed saw and formed into a disk 0.3mm in thickness. The disk was hydrogenated under H_2 gas flowing at room temperature. X-ray diffraction measurement was performed in-situ to monitor a volume expansion during the hydrogenation process. The hydrogen content in the alloy was evaluated using the linear relationship with the lattice constant.

XAS measurements were performed on BL-11 at HiSOR. The XAS spectra at the Pd L_3-edge were recorded using the conversion electron yield method. For the Rh and Ru L_3-edges and the Ag L_2-edge, X-ray fluorescence yield method was employed. The absorbance was measured under He gas flowing or 95%He+5%H_2 mixture gas flowing. It was confirmed that the sample maintained more than 90% of the initial hydrogen content after the XAS measurements.

Figure 1 shows normalized X-ray absorption near edge structure (XANES) profiles of bulk Pd-*M* alloys and the spectra after hydrogenation. The suppression of whiteline (peak A) and appearance of a new peak (peak B) were observed in the spectra of the hydrogenated alloys at the Pd, Ru and Rh L_3-edges. The intensity of whiteline is proportional to a number of 4*d* hole. Therefore, the suppression of whiteline means that 4*d* band near the Fermi energy is additionally occupied after hydrogenation [3]. The peak B is attributed to the 4*d* orbital component in the anti-bonding state with hydrogen atom. Accordingly, Pd, Ru and Rh atoms bonds to hydrogen atom in the Pd-*M* alloy.

There is no whiteline at the Ag L_2-edge because the 4*d* electronic states of Ag is fully occupied. Any remarkable change due to hydrogenation was not observed in Ag L_2-edge. Thus Ag atom does not bond to H atom in the Pd-Ag alloy.

We observed measurable shifts of the absorption edge E_0 after hydrogenation. E_0 was estimated from the first inflection point of the absorption profile. In the case of Pd, E_0 moves to a higher energy, whereas E_0 at the Ru L_3-edge moves to a lower energy after hydrogenation. Figure 2 shows a linear relationship of the shift of E_0 (ΔE_0) at the Pd, Rh, and Ru L_3-edges. Because energy position of the absorption edge is influenced by the screening of the core-hole potential, the linear dependence of ΔE_0 probably demonstrates a systematic change of the electronic structures of Ru, Rh, and Pd in the alloy due to hydrogenation.

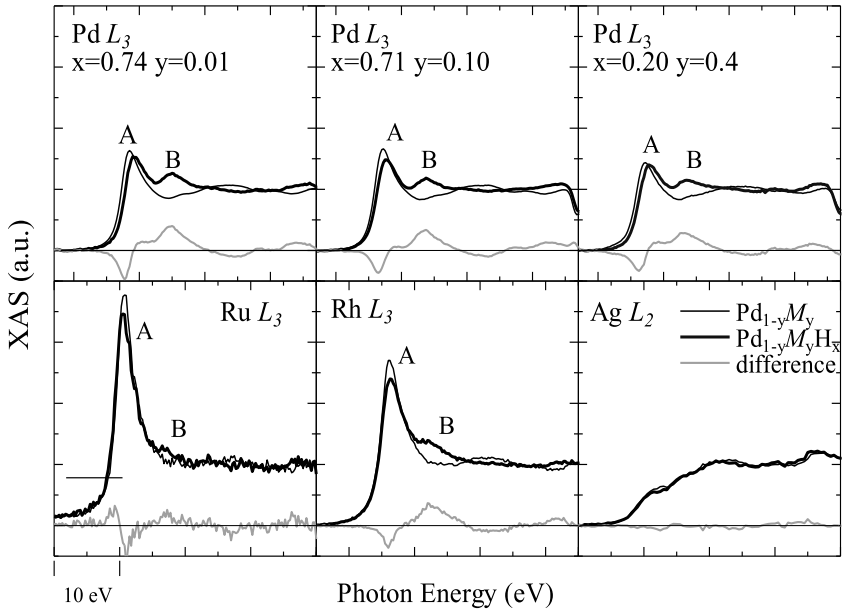

FIGURE 1: XANES profiles of Pd-M (M = Ru, Rh, Ag) alloy (thin lines) and the profiles after hydrogenation (thick lines). The grayish lines show difference between the two spectra.

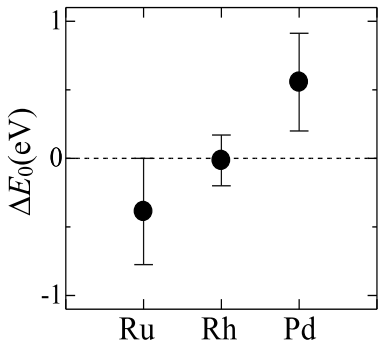

FIGURE 2: Shift of the energy position of the absorption edge (ΔE_0) caused by hydrogenation.

REFERENCES

[1] S. Thiebaut *et al.*, J. Alloys Comp. **231,** 440 (1995).
[2] T. B. Flanagan, D. Wang, and S. Luo, J. Phys. Chem. B **111,** 10723 (2007).
[3] D.A. Papaconstantopoulos *et al.*, Phys. Rev. B, **17**, 141 (1978).

13-B-43

Selective synthesis of CuS and Cu_2S thin films and S K-edge XAFS characterization

Toma Takiguchi[a)], Tomoe Tahara[a)] Naoki Noguchi[a)], Galif Kutluk[b)], Hirofumi Namatame[b)], Shinjiro Hayakawa[a)]

[a)] Department of Applied Chemistry, Graduate School of Engineering, Hiroshima University, Hiroshima, Japan
[b)] Hiroshima Synchrotron Radiation Center, Hiroshima University, Hiroshima, Japan

1. Introduction

Copper sulfide (Cu_xS) is cheap and good conducting material and it is utilized in many fields such as ion selective electrode and solar panels. Cu_xS is typical non-stoichiometric compounds because the oxidation number of Cu can be either +1 or +2[1]. The stoichiometric variation of Cu_xS resulted in the wide range of reported values of indirect band gap, and the selective synthesis of a special phase is attractive to control optical property of Cu_xS. In this work, phase selective synthesis of copper sulfide thin film was investigated, and the deposited films were characterized with X-ray absorption fine structure (XAFS) spectroscopy.

2. Experimental

Copper sulfide thin films were made by the sulfuration of copper thin films in gas phase. In this process, a copper film of 25 nm on a Si or indium-tin-oxide(ITO) coated glass substrate was exposed to hydrogen sulfide evolved from a solution of 50mM Na_2S. The solution was kept in in the three-necked flask, and the pH of the solution was maintained around pKa_1 of hydrogen sulfide (7.04). The rate of the reaction was examined by changing the exposure time up to 300 m. To compare different hydrogen sulfide concentration in gas phase, two types of reaction places were used. One was in the airtight container where the concentration of hydrogen sulfide was relatively low and the other was in the three-necked flask where the concentration was relatively high (Figure 1).

XAFS experiments were performed on the BL-11[2]. The beamline was equipped with a Si(111) double crystal monochromator. X-ray fluorescence yield (XFY) was monitored with a silicon drift detector (SDD), and conversion electron yield (CEY) could be measured simultaneously.

PEC (Photo electrochemical) measurements were carried out to confirm *p* type character of deposited Cu_xS films. A three-electrode cell containing 0.2 M $Eu(NO_3)_3$ was utilized, and a Ag/AgCl electrode and platinum sheet were used as the reference and the counter electrodes. The light from a Xe lamp was irradiated from the back side of the ITO substrate.

The optical transmission measurement was performed using JASCO V-550 with the substrate as the reference.

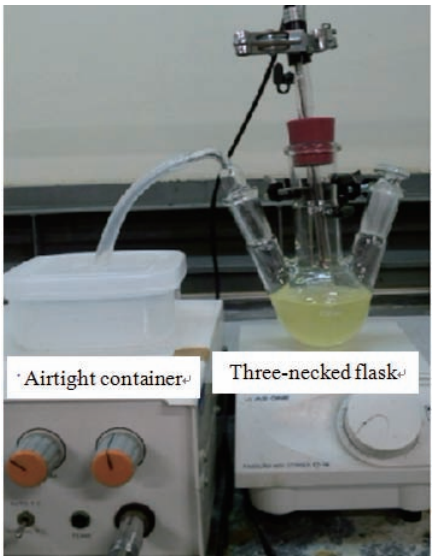

Figure 1.Experimental configuration.

3. Results and Discussion

Figure 2 shows S K-edge XAFS spectra of copper thin films sulfurated under different hydrogen sulfide concentrations with the same exposure time (210 m). Reference spectra were obtained from powders of CuS (P63/mmc) and Cu_2S (P21/c), and the phase of the reference samples were identified with X-ray diffraction (XRD). It was clear that CuS or Cu_2S could be selectively obtained by changing the concentration of hydrogen sulfide. The obtained Cu_2S film was investigated with RBS, and the atomic ratio, Cu/S, was confirmed to be stoichiometric (2.0).

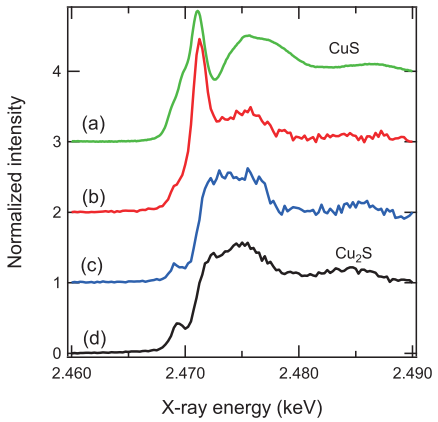

Figure 2 S K-edge XAFS spectra of sulfurated copper films under b) high and c) low hydrogen sulfide concentration. Reference spectra of a)CuS and d) Cu_2S were shown in the same figure.

Figures 3 and 4 show reaction time dependence of XAFS spectra of copper sulfide thin films under the low and high hydrogen sulfide concentrations, and Figures 5 and 6 show reaction time dependence of sulfur XFY under the same condition. All of the spectra shown in Figure 3 and 4 were normalized with the XFY at the incident X-ray energy of 2.490 keV. X-ray energy of 2.490 keV was far from the absorption edge, and the yield was not affected with the chemical state of the sulfur. Therefore, the yield represented amount of the total sulfur.

It was found that all of the spectral profiles were identical to Cu_2S except for the pre-edge region around 2.469 keV in Figure 3. The pre-edge peak was not observed during the initial stage of the reaction when the thickness of the sulfide was steadily growing. The initial product was also Cu_2S in Figure 4, and the pre-edge peak was not observed. However, it was found that spectral shape was gradually transformed from Cu_2S to CuS after the appearance of the pre-edge peak, and the amount of the sulfur started increasing from the middle of the reaction (ca. 200 m). It was found that the over exposure of hydrogen sulfide to the Cu_2S induce the transformation from Cu_2S to CuS.

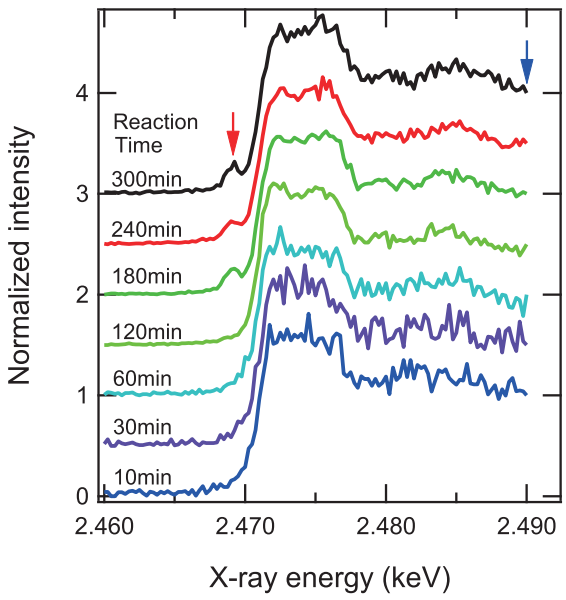

Figure 3 Reaction time dependence of S K-edge XAFS spectra of sulfurated Cu films under low hydrogen sulfide concentration (in the airtight container).

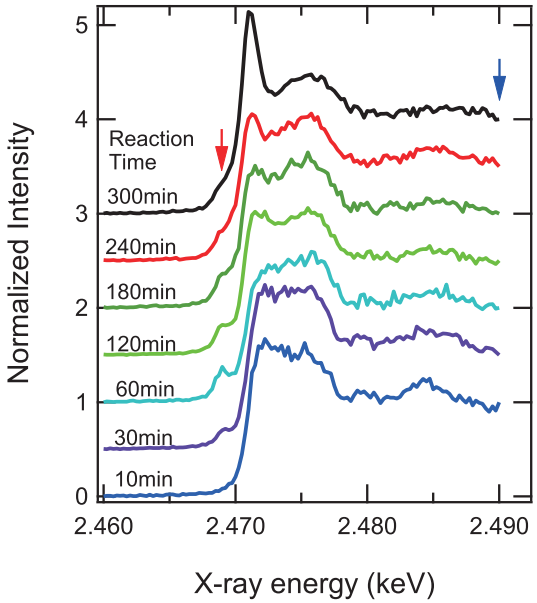

Figure 4 Reaction time dependence of S K-edge XAFS spectra of sulfurated Cu films under high hydrogen sulfide concentration (in the three-necked flask).

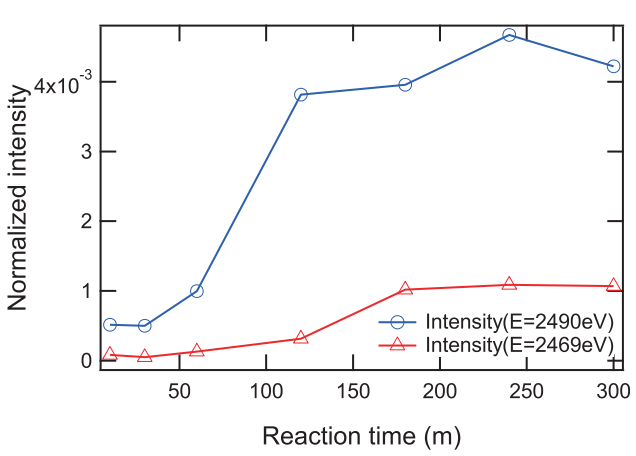

Figure 5 Reaction time dependence of S XFY from obtained with the incident X-ray energy of 2.490 keV (circle) and 2.469 keV (triangle).

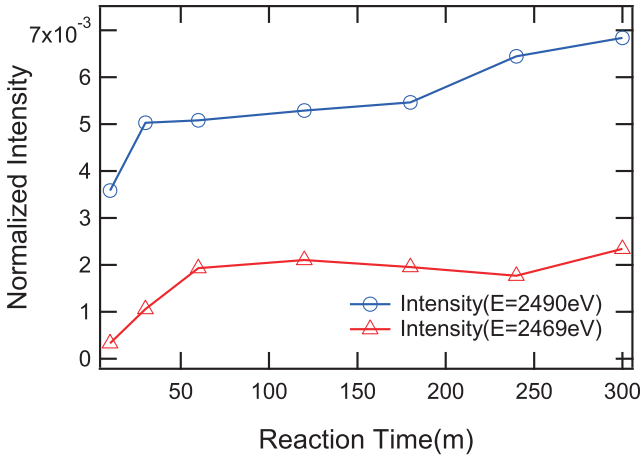

Figure 6 Reaction time dependence of S XFY obtained with the incident X-ray energy of 2.490 keV (circle) and 2.469 keV (triangle).

References
[1]I.Grozdanov et al.,Thin Solid Films,250,67(1994)
[2] S. Hayakawa et al., Anal. Sci., 24, 835-837 (2008).

Development of a coal fly ash and cement mixture for optimum removal of hydrogen sulfide from water

Satoshi ASAOKA[a], Hideo OKAMURA[a] and Shinjiro HAYAKAWA[b]

[a] *Research Center for Inland Seas, Kobe University (5-1-1 Fukaeminami Higashinada Kobe 658-0022 Japan)*
[b] *Graduate School of Engineering, Hiroshima University (1-4-1 Kagamiyama, Higashi-Hiroshima 739-8527 Japan)*

Keywords: eutrophication, enclosed water bodies, environmental remediation, recycled material

1. Introduction

Hydrogen sulfide in eutrophic sediments is highly toxic to benthic organisms and may cause foul odor and blue tide. It is detected in high concentrations in eutrophic enclosed water bodies [1-3]. It is harmful for living organisms because it interferes with cytochrome c oxidase, the last enzyme of the electron transport system [4]. Therefore, it is very important to remove hydrogen sulfide in sediments to maintain healthy ecosystems and support sustainable aquaculture activities. To remediate enclosed water bodies, granulated coal ash was prepared by mixing fly ash from coal electric power plants with cement. However, the best mixture ratio of fly ash and cement has not been optimized. The purpose of this study was to optimize the best mixture ratio of fly ash and cement in terms of hydrogen sulfide removal efficiency.

2. Materials and Methods

Granulated coal ashes with different mixing ratios of fly ash and cement were prepared with added fly ash to cement amounting to 0-97.5% of in final products. These prepared granulated coal ashes were evaluated in terms of hydrogen sulfide removal performances and compression strength.

The hydrogen sulfide solution was prepared as follows: Tris–HCl buffer (Kanto Kagaku) was diluted with ultrapure water to prepare 30 mmol L^{-1} of buffer solution (pH = 8.2). The buffer solution was then deaerated with N_2 gas. Successively, an aliquot of $Na_2S \cdot 9H_2O$ (Wako Pure Chemical Industries) was dissolved to make a solution of 10 mg-S L^{-1}. Fifty milliliters of the hydrogen sulfide solution was slowly dispensed into a 100 mL sealable vial, and 0.2 g of the granulated coal ash was added to the hydrogen sulfide solution. Thereafter, the head space of the bottle was replaced with N_2 gas and the vial was sealed by a rubber cork. Thereafter, it was agitated moderately at 100 rpm at 25ºC in a constant-temperature oven under anoxic condition. The time courses of hydrogen sulfide concentration were measured using a detection tube (200SB: Komyo Rikagaku Kougyo). The batch experiments were conducted in triplicate. Physicochemical parameters such as specific surface area, surface pH and compression strength were also measured.

Sulfur K edge XAFS spectra (ranges 2460–2490 eV) were measured using the BL11 in the Hiroshima Synchrotron Research Center, HiSOR. The synchrotron radiation from a bending magnet was monochromatized with a Si(111) double-crystal monochromator. The sample chamber was filled with He gas, and XAFS spectra were measured by the X-ray fluorescence yield (XFY) mode using a SDD detector (XR-100SDD; AMPTEK). The X-ray energy around K edges of sulfur was calibrated with the spectra of $CuSO_4$ obtained with the CEY mode. The K edge main peak of sulfate was set to 2481.6 eV. The pieces of relatively flat GCA samples were mounted on a double stick tape (NW-K15; Nichiban) placed in the central hole (15 mm in diameter) of a copper plate. The surface of the sample was attached to that of the copper plate. The angle between the incident X-ray and the sample surface was adjusted at 20º, and X-ray fluorescence was detected from the direction normal to the incident beam in the plane of electron orbit of the storage ring.

3. Results and discussion

The removal rate of hydrogen sulfide accelerated with increasing mixing ratio of fly ash. The cement did not adsorb hydrogen sulfide. When the fly ash mixing ratio is over 70%, the hydrogen sulfide removal efficiency was improved. Although the specific surface area reached the maximum at fly ash mixing ratio of 70%, the amount of hydrogen sulfide adsorption increased with increase of the fly ash mixing ratio. Therefore, hydrogen sulfide adsorption was not controlled by specific surface area of the granulated coal ashes. One of the important

factors in hydrogen sulfide adsorption is surface pH of the granulated coal ashes because hydrogen sulfide adsorption on the granulated coal ash competes with OH^-. When the mixing ratio of fly ash is lower than 87%, surface pH of the granulated coal ashes was over 12. On the other hand, in the case of fly ash mixing ratio of more than 87%, the surface pH decreased to between 10.2 and 10.7. When surface pH goes over 12, the OH^- concentration was much higher than that of HS^-, indicating that OH^- competes with HS^- adsorption. In contrast, when the surface pH was less than 11, the OH^- concentration was lower than that of hydrogen sulfide. Therefore, the competition of adsorption between OH^- and HS^- might not be significant.

Compression strength is also very important for field application. When the mixing ratio of fly ash exceeded 95%, the compression strength was significantly decreased for field application even though the amount of hydrogen sulfide adsorption was high. Therefore, the best mixing ratio of the fly ash was estimated to be at 87%.

The sulfur K edge XAFS of the granulated coal ashes (fly ash/cement=87/13) with and without hydrogen sulfide adsorption was measured. The GCA without hydrogen sulfide adsorption had a peak of around 2481.7 eV representing sulfate originating from cement and coal fly ash. After adsorption of hydrogen sulfide the new peak was identified at around 2472 eV representing sulfur. Consequently, the adsorbed sulfur was derived from oxidation of hydrogen sulfide by the granulated coal ash [5].

4. Conclusion

The best mixing ratio of the fly ash was estimated to be at 87% because both the removal performance and compression strength are high at this ratio level.

REFERENCES

1. Reese B.K., Anderson M.A. and Amrhein C., *Sci.Total Environ.* **406**, 205-218(2008).
2. Yamamoto T., Kondo S., Kim K.H., Asaoka S., Yamamoto H., Tokuoka M. and Hibino T., *Mar. Pollut. Bull.* **64**, 2428-2434(2012).
3. Asaoka S., Yamamoto T., Takahashi Y., Yamamoto H., Kim K.H. and Orimoto K., *Interdiscip. Stud. Environ. Chem. Environ. Pollut. Ecotoxicol*. **6**, 345-352(2012).
4. Affonso E.G., Polez V.L.P., Corrêa C.F., Mazon A.F., Araújo M.R.R., Moraes G. and Rantin F.T, *Comp. Biochem. Physiol.* C **139**, 251-257(2004).
5. Asaoka S., Hayakawa S., Kim K.H., Takeda K., Katayama M. and Yamamoto T, J. *Colloid Interf. Sci.* **377**, 284-290(2012).

Acknowledgement

This study was partially supported by the Japan Society for the Promotion of Science JSPS KAKENHI Grant B25740038

14-A-8 (relevant HiSOR proposal number) BL-11 (HiSOR beamline number)

Formation of sulfur compounds on the Granulated Coal Ash covering on organic enriched sediment

Kyunghoi Kim[a], Tamiji Yamamoto[b] and Shinjiro Hayakawa[c]

[a]*Department of Ocean Engineering, Pukyong National University, Busan 738-737, Korea*
[b]*Graduate school of biosphere science, Hiroshima University, Higashi-Hiroshima 739-8528, Japan*
[c]*Graduate school of engineering, Hiroshima University, Higashi-Hiroshima 739-8527, Japan*

Keywords: Sulfur compounds; granulated coal ash; organic enriched coastal sediment

1. Introduction

Hydrogen sulfide is formed in organically enriched sediments through the reduction of sulfate ions by sulfate reducing bacteria under anoxic condition and it is highly toxic and fatal to living organisms, and consumes oxygen when it is oxidized. Thus, it is important to reduce hydrogen sulfide concentration in the sediments to restore and maintain healthy aquatic ecosystems.

Granulated Coal Ash is a product which is the mixture of fly ash and cement as a binder. Previous studies in batch experiments using hydrogen sulfide solution revealed that GCA could effectively reduce hydrogen sulfide; in this process, manganese oxide contained in the GCA may have oxidized the hydrogen sulfide to sulfur (Asaoka et al., 2012).

However, removal mechanism should depend on the sediment conditions such as pH, ORP, and concentration of hydrogen sulfide. In order to develop technology for remediation of organic enriched sediment using GCA, it is necessary to clarify the mechanism of hydrogen sulfide removal with GCA in the condition of organic enriched sediment.

In the present study, we investigated the formation of sulfur compounds onto the GCA covering on organic enriched coastal sediment by XAFS analyses.

2. Materials and methods

The pH and ORP in the sediment of Fukuyama Inner Bay were 6.89 and -402 mV and maximum concentration of hydrogen sulfide in Fukuyama Bay were about 300 mg/l. The Ignition Loss and Particulate Organic Sulfur in the sediment of Fukuyama Inner Bay ranged 10 - 30% and 8 - 18 mg/g, respectively.

GCA samples for XAFS analysis were collected using acrylic pipes (Φ=15 cm, 20 cm long) by a diver at Fukuyama inner bay (Fukuyama GCA) 3 years later the GCA covering was conducted for the sediment remediation. The GCA samples were sealed in a plastic bottle with mud to prevent oxidation after measuring pH and ORP (PS-112C, RM1; TOA Electronics, Ltd., Tokyo, Japan). Sulfur K-edge measurement was carried out using wet GCA immediately after the mud was gently removed with paper.

Sulfur K-edge measurements (range 2460-2485 eV) were made with BL11 in Hiroshima Synchrotron Research Center, HiSOR (Hayakawa et al., 2008). The synchrotron radiation from a bending magnet was monochromatized with a Si(111) double-crystal monochromator. The sample chamber was filled with He gas to suppress any X-ray absorption and scattering from air, and XAFS spectra were measured both by a X-ray fluorescence yield (XFY) mode using a SDD detector (XR-100SDD; AMPTEK) and a conversion electron yield (CEY) mode. The step size for measurement was 0.25 eV. The sulfur K-edge was calibrated with cupric sulfate ($CuSO_4 \cdot 5H_2O$) peak set at 2481.6 eV (Backnaes et al., 2008). As references, humic acid, FeS, MnS were measured by the CEY mode.

XAFS spectra were analyzed with a XAFS spectra processing software (REX2000 ver. 2.5: Rigaku co. Ltd.). A background adsorption was approximated by a least-square fitting. An adsorption edge (E_o) was defined as the inflection point in the spectrum.

3. Results and discussion

The sulfur K-edge XANES spectra were measured for the GCAs (Fig. 1). The initial GCA has a peak at 2482 eV representing sulfate. New peak at 2469 eV was observed for the Fukuyama GCA and the peak at 2482 eV observed for the initial GCA shifted to 2481.5 eV. The peak at 2469 eV is identified as that of FeS, and the shift of the peak from 2482 eV to 2481.5 is judged to be influenced by the peak of FeS (eq 1).

$$Fe^{2+} + HS^- \rightarrow FeS + H^+ \quad (1)$$

New small peak at 2472 eV was observed for Fukuyama GCA. This means that hydrogen sulfide was adsorbed onto the granulated coal ash (MnS) and the oxidation reaction of hydrogen sulfide was coupling with reduction of manganese oxide (eq 2; Asaoka et al., 2012).

$$Mn_2O_3 + H_2S + 4H^+ \rightarrow 2Mn^{2+} + S + 3H_2O \quad (2)$$

Peaks at 2473 eV and 2475.5 is coincided with that of Humic acid indicating adhesion of organic matter.

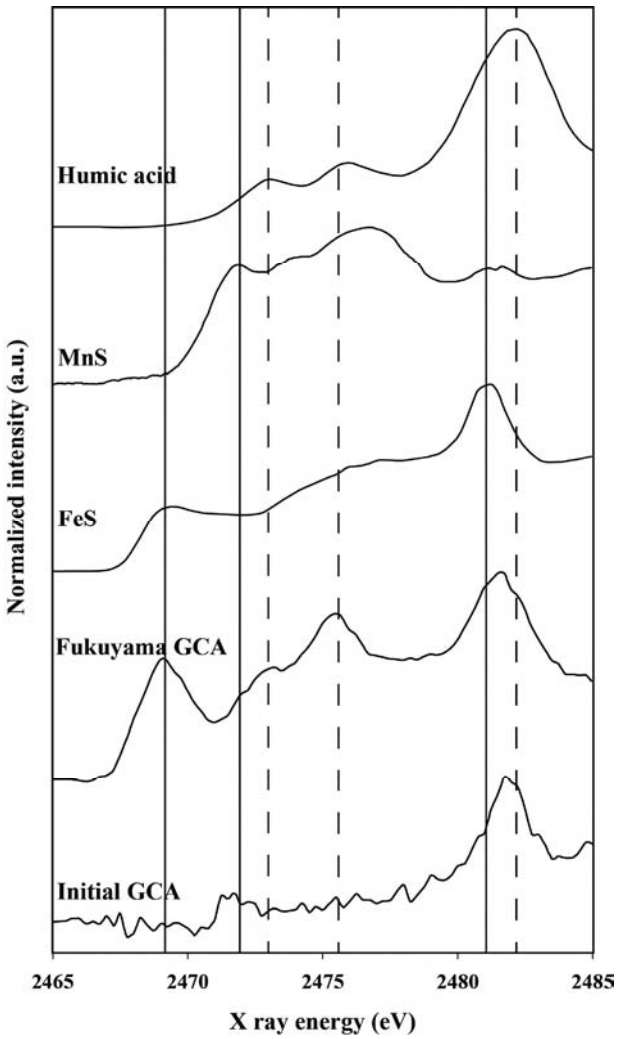

FIGURE 1. Sulfur K-edge XANES spectra of the sampled GCA with several sulfur standards.

REFERENCES

1. S. Asaoka, S. Hayakawa, K.H. Kim, K. Takeda, M. Katayama, and T. Yamamoto, *J. Coll. Int. Sci.***377**, 284-290 (2012).
2. L. Backnaes, J. Stelling, H. Behrens, J. Goettlicher, S. Mangold, O. Verheijen, R. G. C. Beerkens, J. Deubener, *J. American Cer. Soc.* **91**, 721-727 (2008).
3. S. Hayakawa, Y. Hajima, S. Qiao, H. Namatame, and T. Hirokawa, *Anal. Sci.* **24**, 835-837 (2008).

XAFS characterization of copper sulfide thin films

Shinjiro Hayakawa[a)], Yusuke Hayasaka[a)], Tomoe Tahara[a)], Toma Takiguchi [a)], Galif Kutluk[b)], Hirofumi Namatame[b)]

[a)] *Department of Applied Chemistry, Graduate School of Engineering, Hiroshima University, Hiroshima, Japan*
[b)] *Hiroshima Synchrotron Radiation Center, Hiroshima University, Hiroshima, Japan*

1. Introduction

Formation of copper sulfide from copper thin film was conducted with two methods. One was exposure to the hydrogen sulfide gas, and the transformation from Cu_2S to CuS was observed when the formed Cu_2S film was over exposed to the hydrogen sulfide gas [1]. The other method was electrochemical reaction in the solution of $Na_2S_2O_3$. Sulfur K-edge XAFS spectroscopy was utilized to estimate areal density and the chemical state of sulfur on the sample, and the nature of the copper sulfide films were compared between two methods..

2. Experimental

Copper sulfide formation by the gas exposure was reported previously [1]. In the solution process solutions of 0.1 M $Na_2S_2O_3$ and 0.02 M $LiClO_4$ were prepared, and their pH was adjusted to 2.5 and 5.2 with 1 M HCl solution. Electrochemical reaction was took place with the potentiostat system using a standard three electrode electro chemical cell in which the reference electrode was Ag/AgCl and a counter electrode was a Pt plate. A copper plate of 10 mm square was used as a working electrode, and an appropriate potential was applied. The formed film was cleaned with the 1.0 M HCl solution.

XAFS experiments were performed on the BL-11[2]. The beamline was equipped with a Si(111) double crystal monochromator. X-ray fluorescence yield (XFY) was monitored with a silicon drift detector (SDD), and conversion electron yield (CEY) could be measured simultaneously.

3. Results and Discussion

Fig. 1 shows S K-edge XAFS spectra of copper plate before and after the application of the potential of -0.231V (vs. Ag/AgCl) in the neutral solution pH 5.2. The increase of sulfur XFY at the incident X-ray energy of 2.490 keV shows the evidence of the electrochemical reaction of $S_2O_3^{2-}$. Chemisorbed $S_2O_3^{2-}$ was removed after the HCl cleaning, and the XAFS spectrum of the remained phase shown in Fig.2 was identical to that of Cu_2S formed with the exposure to the gas. The difference between these two spectra was pre-edge peak marked in the figure, and it was suggested that the appearance of the pre-edge peak indicate over exposure to the hydrogen sulfide gas resulted in the formation of additional S-S bond in the sample.

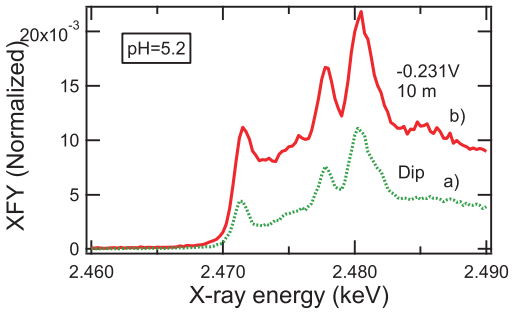

Fig. 1 S K-edge XAFS spectra of copper plate in the solution a) before and b) after the application of the potential of -0.231V (vs. Ag/AgCl)

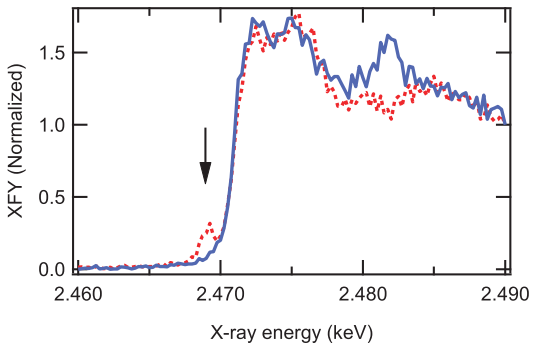

Fig. 2 S K-edge XAFS spectra of Cu2S formed with the exposure to the gas (dotted line) and with the electrochemical reaction (solid line).

References
[1] T. Takiguchi et al., HiSOR Activity report 2013.
[2] S. Hayakawa et al., Anal. Sci., 24, 835-837 (2008).

Investigation of electro-deposition of silver by in-situ XRF measurement

N. Noguchi[a], G. Kutluk[b], H. Namatame[b] and S. Hayakawa[a]

[a] *Department of Applied Chemistry, Graduate School of Engineering, Hiroshima University, Hiroshima, Japan*
[b] *Hiroshima Synchrotron Radiation Center, Hiroshima University, Hiroshima, Japan*

Keywords: electrochemistry, electroplating, silver, in-situ XRF measurement

Electroplating of silver is important in chemical industry. The process of the electroplating with saving energy and cost is required to be high electrical efficiency. The electrical efficiency of the electroplating can be assessed as transport number, which is the ratio of actual thickness of the electrodeposited plate to the thickness estimated from the electric charge amount consumed in a plating process. The thickness of the electrodeposited plate can be estimated from the intensity of the fluorescence X-ray of the silver plate. We examined the transport number of the electroplating of silver by in-situ X-ray fluorescence measurement (XRF) at BL11 of HiSOR.

The electrochemical cell is made of acrylic resin, and it is provided with an X-ray window of 13.0 mm in diameter [1]. The copper thin film deposited on a Kapton film is used as working electrode (WE), and it is fixed on the X-ray window with an O-ring. A Pt plate is served as the counter electrode (CE) and the reference electrode (RE) is Ag/AgCl electrode. The potential is applied to the WE using a potentiostat (HAL 3000, Hokuto Denko Co.). The texture of the electrodeposited silver plate was monitored with a USB camera. The angle between the incident X-ray and the window of the cell was 45 degrees, and the fluorescence X-ray was detected from the direction normal to the incident X-ray. The fluorescence X-ray of Ag-Lα emission line was measured using a single element SDD (Super SDD, Amptek Co.) and a digital pulse processor (PX4, Amptek Co.) .

To construct a calibration curve, the fluorescence X-ray of Ag films whose thicknesses were known were measured. The calibration curve is shown in Fig. 1. It is the function of the intensity of Ag-Lα line as the thickness of Ag film. $AgNO_3$ of 0.01-0.1M was dissolved in plating solutions. 0.02-0.1 M EDTA and 0.02-0.1 M $NaNO_3$ solution of pH 10-11.5 were used as complexing agent and electrolyte, respectively [2]. The voltage of -0.2 V was applied to WE. The Ag was deposited uniformly on the WE. The intensity of Ag-Lα line was increased with time (Fig. 2). The thickness of Ag film was determined from the intensity using the calibration curve (Fig. 3), and the transport number was estimated. The transport numbers were changed in the range from 0.09 to 0.7, and it is increased with increasing the ratio of $NaNO_3$ to $AgNO_3$. The result shows the transport number is depending on the concentration of electrolyte.

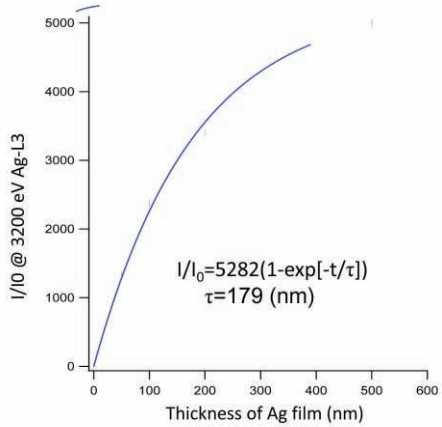

Fig.1 Calibration curve for thickness of Ag film.

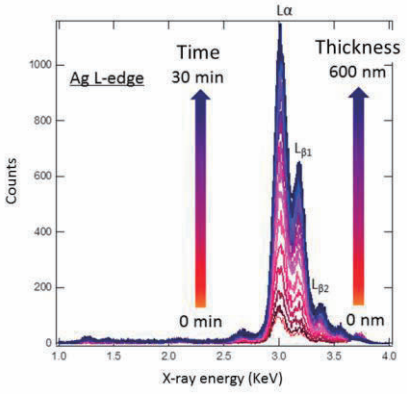

Fig.2 In-situ XRF spectra during electroplating of Ag.

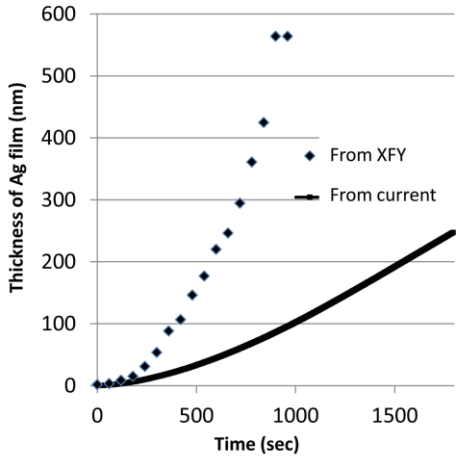

Fig.3 Change of thickness of Ag film with time.

REFERENCES

1. N.Noguchi, T. Takiguchi, G. Kutluk, H. Namatame, S Hayakawa, The 18th HiSOR symposium, 13-B-45 (2014)
2. G.M. de Oliveira, L.L Barbosa, R.L. Broggi, I.A. Carlos, *J. Electroanal. Chem.* **578**, 151-158 (2005)

Characterization of Intermolecular Structure of β_2-Microglobulin Core Fragments in Amyloid Fibrils by Vacuum-Ultraviolet Circular Dichroism Spectroscopy and Circular Dichroism Theory

Koichi Matsuo,[a,b] Hirotsugu Hiramatsu,[c] Kunihiko Gekko,[d] Hirofumi Namatame,[a] Masaki Taniguchi,[a] and Robert W. Woody[b]

[a] *Hiroshima Synchrotron Radiation Center, Hiroshima University, Higashi-Hiroshima 739-0046, Japan*
[b] *Department of Biochemistry and Molecular Biology, Colorado State University, Fort Collins, CO 80523, USA*
[c] *Graduate School of Pharmaceutical Sciences, Tohoku University, Sendai 980-8578, Japan*
[d] *Department of Mathematical and Life Sciences, Graduate School of Science, Hiroshima University, Higashi-Hiroshima 739-8526, Japan*

Keywords: Molecular dynamics simulation, Phe-Tyr interaction, Synchrotron-radiation circular dichroism spectroscopy.

Intermolecular structures are important factors for understanding the conformational properties of amyloid fibrils. In this study, vacuum-ultraviolet circular dichroism (VUVCD) spectroscopy and circular dichroism (CD) theory were used for characterizing the intermolecular structures of β_2-microglobulin (β_2m) core fragments in the amyloid fibrils. [1] The VUVCD spectra of β_2m_{20-41}, β_2m_{21-31}, and β_2m_{21-29} fragments [2, 3] in the amyloid fibrils exhibited characteristic features, but they were affected not only by the backbone conformations but also by the aromatic side-chain conformations. To estimate the contributions of aromatic side-chains to the spectra, the theoretical spectra were calculated from the simulated structures of β_2m_{21-29} amyloid fibrils with various types of β-sheet stacking (parallel or anti-parallel) using CD theory [4, 5]. We found that the experimental spectrum of β_2m_{21-29} fibrils is largely affected by aromatic-backbone couplings which are induced by the interaction between transitions within the aromatic and backbone chromophores, and these couplings are sensitive to the type of stacking among the β-sheets of the fibrils. Further theoretical analyses of simulated structures incorporating mutated aromatic residues suggested that the β_2m_{21-29} fibrils are composed of amyloid accumulations in which the parallel β-sheets stack in an anti-parallel manner and that the characteristic Phe-Tyr interactions among the β-sheet stacks affect the aromatic-backbone coupling. These findings indicate that the coupling components, which depend on the characteristic intermolecular structures, induce the spectral differences among three fragments in the amyloid fibrils. These advanced spectral analyses using CD theory provide a useful method for characterizing the intermolecular structures of protein and peptide fragment complexes.

REFERENCES

1. K. Matsuo. H. Hiramatsu, K. Gekko, H. Namatame, M. Taniguchi, and R. W. Woody, *J. Phys. Chem. B*, *in press*.
2. H. Hiramatsu, Y. Goto, H. Naiki, and T. Kitagawa, *J. Am. Chem. Soc.*, **127**, 7988−7989 (2005).
3. H. Hiramatsu, Y. Goto, H. Naiki, and T. Kitagawa, *Bull. Chem. Soc. Jpn*. **83**, 495**–**504 (2010).
4. N. Sreerama and R. W. Woody, *Methods Enzymol.*, **383**, 318−351 (2004).
5. R. W. Woody, *J. Am. Chem. Soc.*, **131**, 8234−8245 (2009).

Conformation Analysis of Membrane-Bound Proteins by Vacuum-Ultraviolet Circular-Dichroism and Linear-Dichroism Spectroscopy

Koichi Matsuo,[a] Hirofumi Namatame,[a] Masaki Taniguchi,[a] Kunihiko Gekko[b]

[a]*Hiroshima Synchrotron Radiation Center, Hiroshima University, Higashi-Hiroshima 739-0046, Japan*
[b]*Institute for Sustainable Sciences and Development, Hiroshima University, Higashi-Hiroshima 739-8526, Japan*

Keywords: Liposome; Molecular orientation; Protein–membrane interaction; Secondary structure; Synchrotron radiation.

Knowledge of the conformations of membrane-bound proteins is important to understand the mechanism of protein–membrane interaction and the biological function of proteins in a biomembrane envirommment [1,2]. We applied the vacuum-ultraviolet circular-dichroism (VUVCD) [3] and linear-dichroism (LD) spectroscopy [4] to analyze the conformational changes of α-lactalbumin (LA), thioredoxin (Trx), and β-lactoglobulin (LG) induced by the interaction with phosphatidylglycerol liposome [5]. The VUVCD analysis [6] showed that the three proteins had characteristic helical conformations in the presence of liposome, significantly increasing the length and number of α-helix segments compared to those in the native states. The amino acid sequences of proteins interacting with liposome were predicted by the net charge and hydrophobicity of each helix segment, and the orientations of the helix segments in or on the liposome were determined by the LD analysis under a shear-flow condition. It was found that, in the membrane-bound states, LA had two amphiphilic helices stretched on the liposome surface, whereas Trx and LG had two and one hydrophobic helices, respectively, which were vertically penetrated into the liposome (lipid bilayer). These results demonstrate that the combination method of VUVCD and LD is useful for analyzing the conformations of membrane-bound proteins, which are linked to the membrane-mediated physiological function of proteins.

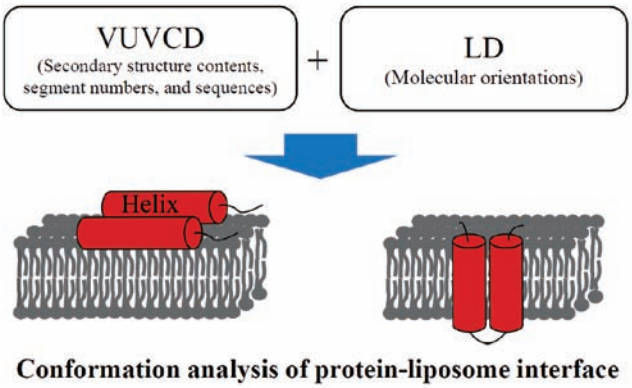

Conformation analysis of protein-liposome interface

REFERENCES

1. Bourdineaud, J. P.; Boulanger, P.; Lazdunski, C.; Letellier, L. *Proc. Nat. Acad. Sci. USA* **1990**, *87*, 1037–1041.
2. Tsurudome, M.; Gluck, R.; Graf, R.; Falchetto, R.; Schaller, U.; Brunner, J. *J. Biol. Chem.* **1992**, *267*, 20225−20232.
3. Ojima, N.; Sakai, K.; Matsuo, K.; Matsui, T.; Fukazawa, T.; Namatame, H.; Taniguchi, M.; Gekko K. *Chem. Lett*. **2001**, *30*, 522–523.
4. Hicks, M. R.; Dafforn, T. R.; Damianoglou, A.; Wormell, P.; Rodger, A.; Hoffman, S. V. *Analyst* **2009**, *134*, 1623–1628.
5. Matsuo, K.; Namatame, H.; Taniguchi, M.; Gekko, K. *Biochemistry* **2009**, *48*, 9103–9111.
6. Matsuo, K.; Yonehara, R.; Gekko, K. *J. Biochem*. **2004**, *135*, 405–411.

VUV-CD measurements of modified histone proteins

Yudai Izumi[a], Kentaro Fujii[a], Koichi Matsuo[b], and Akinari Yokoya[a]

[a]*Advanced Science Research Center, Japan Atomic Energy Agency, Ibaraki, Japan*
[b]*Hiroshima Synchrotron Radiation Center, Hiroshima University, Hiroshima, Japan*

Keywords: histone, chemical modification, DNA damage responses, vacuum ultraviolet circular dichroism

DNA wraps around core histone proteins composed of several subunits, named as H2A, H2B, H3, and H4, in eukaryotic nuclei. DNA damage may cause alterations of the genetic codes. Living organisms have evolved the system to detect and repair DNA damage. Recent studies showed the chemical modifications of histone proteins play important roles in DNA repair processes [1-3].

Recently, we observed relative increment of α-helix structure of histone H2A/H2B induced by X-ray irradiation to human cells using circular dichroism (CD) spectroscopy [4]. In an attempt to examine secondary structural change of histone H3/H4, we measured vacuum ultraviolet CD (VUV-CD) spectra of H3/H4 extracted from X-irradiated and unirradiated human cells. Here, we report preliminary VUV-CD spectra of H3/H4.

HeLa. S-FUCCI cells were cultured in several culture dishes (*ca.* 1×10^7 cells/dish). The cells in culture dishes were irradiated with 40 Gy X-rays. After irradiation, the cells were incubated at 37°C in a humidified atmosphere of 5% CO_2 and 95% air for 30 minutes to progress DNA repair pathway. Histone H3/H4 was extracted from X-irradiated and unirradiated cells using Histone Purification Kit (Active Motif) and dissolved with 10 mM Tris-HCl buffer (pH = 8.0) and 250 mM NaF. VUV-CD measurements were carried out at BL-12 of HiSOR. The samples were kept at room temperature during the measurements.

Figure 1 shows VUV-CD spectra of irradiated and unirradiated samples. Both spectra show three CD peaks at around 190, 208, and 222 nm. Those peaks are characteristic CD peaks of α-helix structure. It shows that the main structure of H3/H4 is α-helix. Since spectral difference around 205-230 nm was within the error bars (Fig. 1 inset), apparent difference between unirradiated and X-irradiated samples was not observed. This result suggests that (1) the structure of H3/H4 was not altered in this experimental condition although that of H2A/H2B was altered, or (2) opposite structural changes between H3 and H4 occurred, for example, α-helix structure of H3 increased, but that of H4 decreased, since CD spectra reflect total amount of each secondary structure. In order to confirm that, it is necessary to measure VUV-CD spectra of H3 and H4 separately.

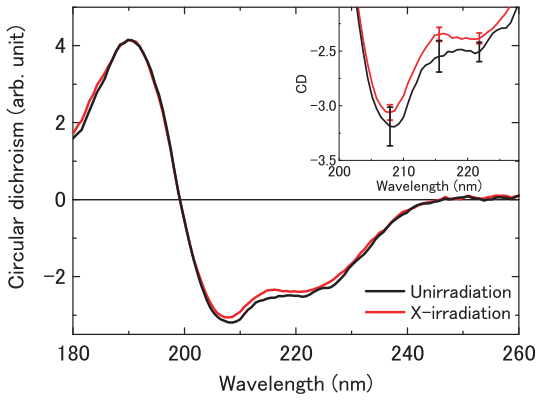

FIGURE 1. VUV-CD spectra of histone H3/H4 extracted from unirradiated and X-irradiated cells. Inset right above shows magnification of the spectra around 200-230 nm with partial error bars.

REFERENCES

1. B. D. Price and A. D. D'Andrea, *Cell* **152**, 1344-1354 (2012).
2. C. R. Hunt *et al*., *Rad. Res.* **179**, 383-392 (2013).
3. F. Gong and K. M. Miller, *Mutat. Res.-Fund. Mol. Mech. Mutagen.* **750**, 23-30 (2013).
4. Y. Izumi *et al*., Abstract book of Asia-Pacific Symposium on Radiation Chemistry 2014 (P-34).

Effect of Molecular Weight on Synergy in Mixed Gels of κ-Carrageenan and Locust Bean Gum Studied by Vacuum Ultraviolet Circular Dichroism

Yasuyuki Maki[a], Kazushi Toriba[a], Kazuya Ishizaka[a], Hiroyuki Yoshida[a], Sho Yasuraoka[a], and Koichi Matsuo[b]

[a]*Division of Molecular Science, Graduate School of Science and Technology, Gunma University, Kiryu 376-8515*
[b]*Hiroshima Synchrotron Radiation Center, Hiroshima University, Higashi-Hiroshia 739-8526*

Keywords: synergistic effect, mixed gel, polysaccharides, vacuum ultraviolet circular dichroism

A range of proteins, polysaccharides and their mixtures are employed as gelling agents by the food industry. In many cases, gelation of these food macromolecules is accompanied by conformational transition of macromolecules, which is induced by temperature, pressure, pH, etc. Vacuum-ultraviolet circular dichroism (VUVCD) is an effective tool for assignment of structures and conformational change of polysaccharides and proteins [1]. Gels used in foodstuffs are usually multi-component systems such as mixtures of proteins and polysaccharides. In some cases, the mixed gels show a synergistic effect, that is, enhanced rheological properties at a certain mixing ratio holding the total polymer concentration constant or gelation at concentrations below the gelation concentration of pure components. The synergistic effect is applied to gelling agents used in food industries.

κ-Carrageenan is a polysaccharide extracted from red marine algae and is composed of alternating disaccharide units of (1→3)-linked β-D-galactose-4-sulphate and (1→4)-linked 3,6-anhydro-α-D-galactose. This polymer shows a coil-helix conformation transition. At lower temperatures, κ-carrageenan molecules form double-helices and then the gel network is formed in the presence of potassium ions [2]. Galactomannans are extracted from the endosperms of legume seeds and are composed of a (1→4) linked β-D-mannan backbone partially substituted at C-6 with α-D-galactosyl residues. Galactomannans are water-soluble and do not form gels. It has been known that mixtures of κ-carrageenan and galactomannan form thermoreversible gels and the mixed gels show a synergistic effect, an enhancement of the gel strength at a certain mixing ratio of κ-carrageenan and galactomannan [2]. It was suggested that the intermolecular binding creates more cross-links in the mixed gel. Investigations of the mixed systems with NMR [3] and light scattering [4] supported the concept of the binding between the two polysaccharides. In the studies of X-ray fiber diffraction of oriented fibers prepared from mixed gels, unique X-ray patterns corresponding to a specific interaction between the two polysaccharides were not observed [2]. The molecular conformations of κ-carrageenan and galactomannan in the mixed gels have not been clarified. In the previous study [5], we investigated the conformations of the two polysaccharides in the mixed gels by using VUVCD, and observed that there is no difference of polysaccharide conformations between in the mixed gel and in the pure systems. This study is aimed at clarifying the effect of molecular weight of galactomannan on the synergistic effect of the mixed gel by use of mechanical tests and VUVCD spectroscopy.

Sodium κ-carrageenan was provided by MRC Polysaccharide Co. Ltd., Japan. Two locust bean gum samples with different molecular weights were used as galactomannan samples. One of the samples (LBG-L) was purchased from Wako Pure Chemical Industries, Ltd., Japan ($M_v \sim 5 \times 10^5$), and the other (LBG-H) was provided by CP Kelco Japan ApS ($M_v \sim 1 \times 10^6$). κ-Carrageenan and galactomannan were dissolved in 10 mM KCl solution to be solutions of various mixing ratios of κ-carrageenan and galactomannan holding the total polymer concentration to be 1.6 wt%. Uniaxial compression tests of mixed gels were carried out with a universal testing machine (Ez-Test, Shimadzu) and the fracture stress σ_f of the gels was determined. The VUVCD spectra of mixed gels were measured from 220 nm to 175 nm under a nitrogen atmosphere by use of the VUVCD spectrophotometer constructed at Hiroshima Synchrotron Radiation Center (BL-12) and an

assembled-type optical cell at 25 °C. The path length of the cell was adjusted with a Teflon spacer to 10 μm [1, 6].

The fracture stress σ_f of the mixed gel as a function of a weight fraction w_{LBG} of galactomannan showed a peak at $w_{LBG} \sim 0.5$, indicating an enhancement of the gel strength by mixing (synergistic effect). The synergistic effect of the mixed gel of LBG-H was more significant than that of LBG-L: the value of σ_f at the peak for LBG-H was larger than that for LBG-L.

The measured VUVCD spectra of a κ-carrageenan gel and of a galactomannan solution showed a negative peak at 181 nm and a positive peak at 179 nm, respectively, as was reported previously [7, 8]. The spectra of the mixed gels varied with the mixing ratio. Figure 1 shows the ellipticity θ_{180} at 180 nm as a function of w_{LBG}. The linear relation between θ_{180} and w_{LBG} was observed for both LBG-L and LBG-H, and was consistent with the mixing rule of the spectra: [5]

$$\theta(\lambda) = w_{LBG}\theta_{LBG}(\lambda) + (1 - w_{LBG})\theta_{CAR}(\lambda), \quad (1)$$

where θ_{LBG} and θ_{CAR} are the spectrum for galactomannan and the spectrum for pure κ-carrageenan, respectively. This result indicates that there is no difference of polysaccharide conformations between in the mixed gel and in the pure systems, and a specific conformation corresponding to the intermolecular binding of the two polysaccharides is not formed. The present study confirmed a swollen network picture [2] for the mixed gel where κ-carrageenan forms a network and galactomannan resides within and swells the network, and showed that this picture was independent of the molecular weight of galactomannan.

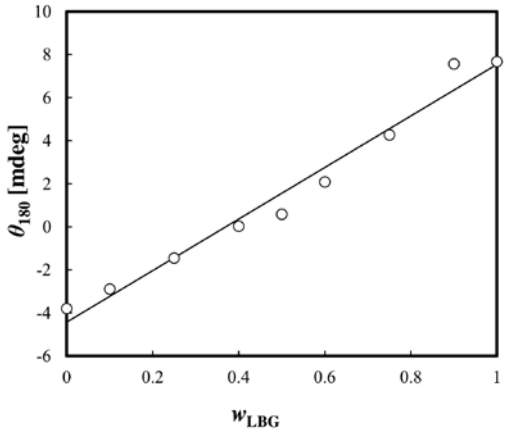

FIGURE 1. The ellipticity θ_{180} at 180 nm for the mixed gel containing LBG-H plotted against weight fraction w_{LBG} of locust bean gum.

Acknowledgements This work was supported by JSPS KAKENHI (Grants-in-Aid for Scientific Research) Grant Number 25870111.

REFERENCES

1. N. Ojima, K. Sakai, K. Matsuo, T. Matsui, T. Fukazawa, H. Namatame, M. Taniguchi and K. Gekko, Chem. Lett. 30, 522 (2001).
2. V. J. Morris, "Gelation of Polysaccharides" in Functional Properties of Food Macromolecules, 2nd edition, edited by S. E. Hill, D. A. Ledward and J. R. Mitchell, Gaithersburg: Aspen Publishers, Inc., 1998.
3. T. Turquois, C. Rochas and T. Taravel, Carbohydr. Polym. 17, 263 (1992).
4. C. Viebke and L. Piculell, Carbohydr. Polym. 29, 1 (1996).
5. Y. Maki, S. Yasuraoka, K. Toriba and K. Matsuo, HiSOR Activity Report 2013.
6. K. Matsuo, K. Sakai, Y. Matsushima, T. Fukuyama and K. Gekko, Anal. Sci. 19, 129 (2003).
7. L. A. Buffington, E. S. Stevens, E. R. Morris and D. A. Rees, Int. J. Biol. Macromol. 2, 199 (1980).
8. E. R. Arndt and E. S. Stevens, Carbohydr. Res. 303, 73 (1997).

Determination of Absolute Configuration for a Natural Product Niphateolide A by Vacuum-Ultraviolet Circular Dichroism

Tatsuo Nehira[a] and Koichi Matsuo[b]

[a]*Graduate School of Integrated Arts and Sciences, Hiroshima University, 1-7-1 Kagamiyama, Higashi-Hiroshima, 739-8521, Japan*
[b]*Hiroshima Synchrotron Radiation Center, Hiroshima University, 2-313 Kagamiyama, Higashi-Hiroshima, 739-0046, Japan*

Keywords: vacuum-ultraviolet electronic circular dichroism, ECD analysis.

On the course of our search for useful natural products, a new diterpene, niphateolide A (**1**), was isolated as an inhibitor of the p53-Hdm2 interaction [1]. For determining the absolute configuration, an electronic circular dichroism (ECD) analysis with the help of theoretical ECD prediction was helpful [2].

Compound **1** was an inseparable stereoisomeric mixture at C-17 with a flexible side chain C-1/C-2/C-3/C-4 (**Fig. 1**) so that the ECD analysis was conducted by integrating a virtual equilibrium between the simplified two forms 10*R*,11*R*,17*R*- and 10*R*,11*R*,17*S*-**1a** with the theoretically-derived internal and free energies [1].

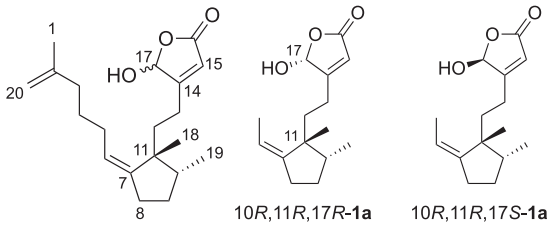

FIGURE 1. Structures of niphateolide A (**1**) and simplified forms **1a**.

We adopted vacuum-ultraviolet electronic circular dichroism (VUV-ECD) [3] for observing ECD down to 180 nm. Since the calculated ECD spectrum for 10*R*,11*R*-**1a** reproduced the experimental ECD spectrum (**Fig. 2**), the absolute configuration of **1** was determined to be 10*R*,11*R*.

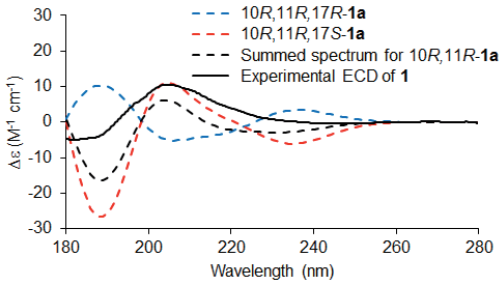

FIGURE 2. VUV-ECD spectrum of **1** along with calculated ECD spectra of **1a**.

REFERENCES

1. H. Kato, T. Nehira, K. Matsuo, T. Kawabata, Y. Kobashigawa, H. Morioka, F. Losung, R. E. P. Mangindaan, N. J. de Voogd, H. Yokosawa, and S. Tsukamoto, *submitted*.
2. H. Takekawa, K. Tanaka, E. Fukushi, K. Matsuo, T. Nehira, and M. Hashimoto, *J. Nat. Prod.* **2013**, *86*, 2503.
3. K. Gekko and K. Matsuo, *Chirality*, **2006**, *18*, 329.

Study of Ion Desorption Dynamics of Methyl-Ester Terminated SAMs Induced by Resonant Core-Excitations

S. Hosoda[a], S. Wada[a,b], R. Koga[a], J. Kajikawa[a], H. Hayashita[a], and A. Hiraya[a,b]

[a] *Department of Physical Science, Hiroshima University, Higashi-Hiroshima 739-8526, Japan*
[b] *Hiroshima Synchrotron Radiation Center, Hiroshima University, Higashi-Hiroshima 739-0046, Japan*

Keywords: Self-assembled monolayers (SAMs), Near edge X-ray absorption fine structure (NEXAFS), Site-selective bond breaking

Core-electron excitations have quite unique nature differently from valence excitations because of special localization of core electrons. So, ion desorption induced by resonant core-excitations also reveals characteristic phenomena, in particular site-selective ionic dissociation is one of noteworthy characteristics.

Recently, it was found that site-selective ion desorption takes place at resonant core excitations of C1s, O1s(OCH_3) → σ^*(O-CH_3) and O1s(OCH_3) → σ^*(C-OCH_3) in methyl ester terminated aliphatic self-assembled monolayer (MHDA-SAM, $CH_3OCO(CH_2)_{15}SH$) [1]. Selective chemical bond breaking is achieved by core-electron excitation due to its localization and atomic selectivity. In the core-excitation of C1s(OCH_3) → σ^*(O-CH_3), such SAMs indicate selective desorption not only for CH_3^+ ion but also for its fragments CH_n^+ (n=0-2) ions. The following studies also revealed the site-selective ion desorption for methyl ester terminated aromatic SAMs, which make higher selectivity than aliphatic SAMs. Fragmentation of selectively desorbing CH_n^+ (n=0-3) ions from aromatic SAMs is heavier than those from aliphatic SAMs.

In this study, site-selective ion desorption from core-excited methyl ester-terminated aliphatic and aromatic SAMs was investigated and desorption mechanism was discussed based on statistical considerations.

Near-edge X-ray absorption fine structure (NEXAFS) measurements were performed at the beamline BL-13 of HiSOR. During measurements, the experimental chamber had a base pressure of 2×10^{-9} Torr. NEXAFS around the C K edge was recorded in total electron yield (TEY) mode by measuring a sample drain current. Partial ion yield (PIY) measurements were carried out at the beamline BL7A of PF during single-bunch operation. PIY spectra were measured by detecting selected ions using a time-of-flight (TOF) mass spectrometer. SAMs were prepared by immersing Au substrates into 1.0 mM ethanol solutions of MHDA ($HS(CH_2)_{15}COOCH_3$), MP0 ($HSPhCOOCH_3$), MP1 ($HSCH_2PhCOOCH_3$) and M2P ($HSPhPhCOOCH_3$). Fig. 1 shows schematic drawings for SAMs used in this experiments. All samples have –$COOCH_3$ at their head groups, connected by phenyl ring(s) with conductivity for MP0, MP1 and M2P SAMs, while MHDA has not conductivity due to aliphatic methylene chain.

Fig. 2(a) shows typical example of site-selective ion desorption measured for MHDA SAM in the C K edge. Differently from the absorption profile (TEY spectrum in upper panel), ion yields of CH_n^+ indicate strong enhancement only in the C1s(OCH_3) → σ^*(O-CH_3) excitation. Such selectively enhanced yields of CH_n^+ are plotted for MHDA, M2P, MP1, and MP0 SAMs in Fig. 2(b), together with the yields in the σ^*(C-C) excitation for easy comparison (Fig. 2(c)). Ion yield ratio in the selective σ^*(O-CH_3) excitation for all SAMs shows strong fragmentation of the CH_3 moiety in desorbing by comparing with that in the non-selective σ^*(C-C) excitation. Such results mean that an available energy produced during the reaction is possessed in the desorbing CH_3 and the available energy is higher in the site-selective σ^*(O-CH_3) excitation than that in the σ^*(C-C) (non-selective) excitation.

In order to understand the reaction dynamics of site-selective

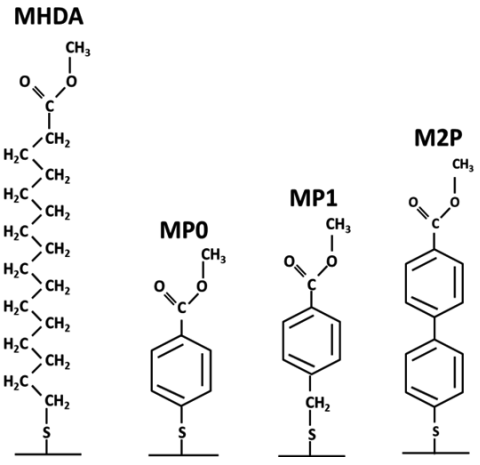

FIGURE 1. Molecular structure of SAMs used in this study, MHDA, MP0, MP1, and M2P.

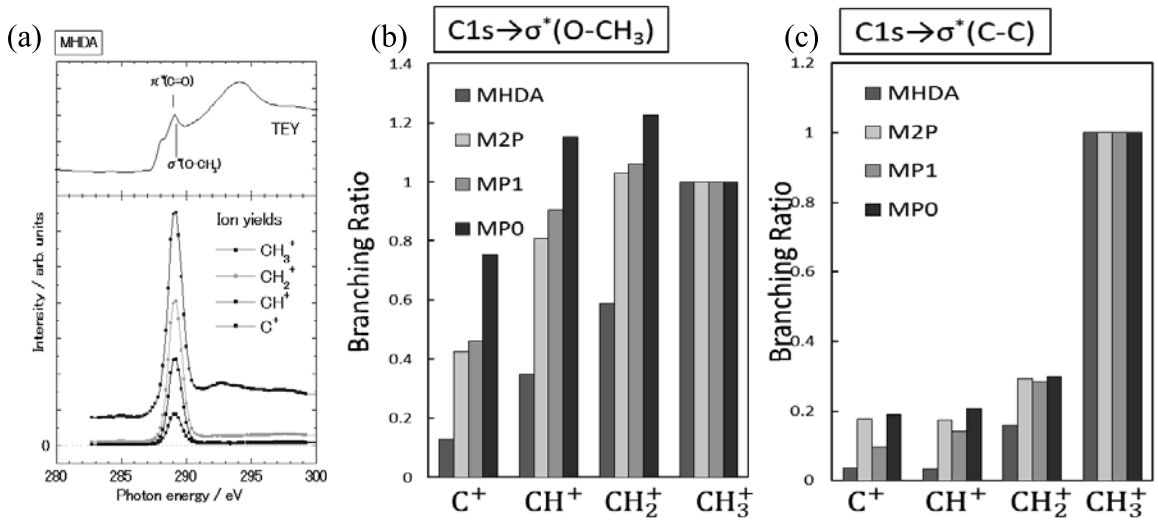

FIGURE 2. (a) Typical TEY and PIY spectra measured for MHDA SAM in the C K edge. Ion yield ratio (branching ratio) of the desorbing CH_n^+ (n=0-3) ions measured for MHDA, M2P, MP1, and MP0 SAMs in the (b) site-selective σ*(O-CH_3) and (c) non-selective σ*(C-C) excitations.

bond breaking accompanied by such fragmentation, ion yield ratio was reproduced under statistical considerations using only one parameter, an available energy E. In this situation, only quantum state-counting is required since the statistical expectation is to populate every energetically allowed product states with a probability proportional to the number of such states, which are permitted by energy conservation. Using this definition of the statistical distribution, the problem is reduced to calculate the density of states for each energetically accessible electronic and vibrational levels of product CH_n^+.

Fig. 3 depicts ion yield ratio of photodesorbing CH_n^+ ions measured for MHDA, M2P MP1, and MP0 SAMs in the site-selective σ*(O-CH_3) and non-selective σ*(C-C) excitation, together with the calculated statistical population ratio based on the listed available energy E. The calculated ratio well reproduces the experimental one; fragmentation in the σ*(O-CH_3) excitation is heavy with high E, while the σ*(C-C) excitation makes soft fragmentation due to low E. Moreover, different yield profile in the σ*(O-CH_3) excitation also reproduced only by changing E depending on conductivity of molecular skeleton; most conductive MP0 SAM shows heaviest fragmentation with highest E, while non-conductive aliphatic SAM MHDA indicates less fragmentation due to lower E. Such relationship between molecular conductivity and site-selectivity (degree of fragmentation) reflects reaction dynamics in breaking chemical bond selectively by resonant core-excitation and the following desorbing process.

References

1. S. Wada, H. Kizaki, Y. Matsumoto, R. Sumii and K. Tanaka, *J. Phys.: Condens. Matter* **18**, S1629-S1653 (2006).
2. J.I. Steinfeld, J.S. Francisco and W.L. Hase, *Chemical Kinetics and Dynamics*, Prentice-Hall, 1998.

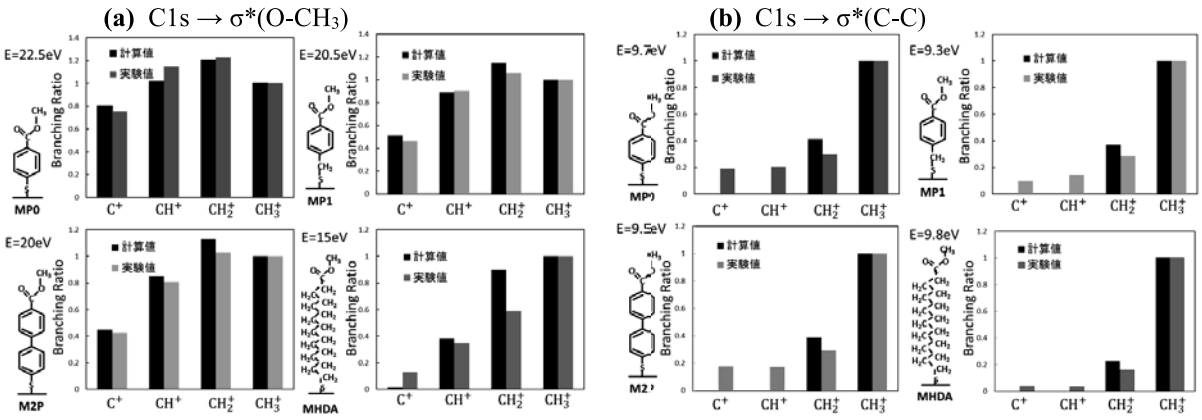

FIGURE 3. Measured and calculated ion yield ratio (branching ratio) of the desorbing CH_n^+ (n=0-3) ions for MHDA, M2P, MP1, and MP0 SAMs in the (a) site-selective σ*(O-CH_3) and (b) non-selective σ*(C-C) excitations. Estimated available energy is also listed in each panel.

Study of self-assembled monolayer of phosphorescent molecule

S. Yamahira[a], K. Yamamoto[a], K. Miyatake[a],
S. Wada[a, b], T. Sekitani[a, b], A. Hiraya[a, b]

[a]*Department of Physical Science, Hiroshima University, Japan*
[b]*Hiroshima Synchrotron Radiation Center, Hiroshima University, Japan*

Keywords: self-assembled monolayer, NEXAFS, phosphorescence

The organothiol self-assembly on metal surface have attracted much interest in a facile manipulating of surface functionality. Phosphorescent molecules have excited triplet state by valence excitation, which has 10^5-10^8 times longer lifetime than singlet excited state of same electronic configuration. This long-lived triplet excited state makes it possible to a formation of doubly-excited state by subsequent core excitation. This excited state is a strongly anti-bonding core-excited state which is expected to open a new reaction channel.

In this study, self-assembled monolayer (SAM) of 4-mercaptobenzoic acid (MBA) is used. Benzoic acid shows phosphorescence with a high quantum yield [1]. The SAM was prepared by immersing the gold coated substrate to 1mM solution in ethanol.

At first, the orientation of SAM was examined by NEXAFS spectroscopy. The NEXAFS measurement was performed at BL13 of Hiroshima Synchrotron Radiation Center. Figure 1 shows NEXAFS spectrum of MBA SAM measured at incident angle of 90 degree. The sharp peak A is assigned to π^* resonant excitation of aryl ring. This peak shows strong polarization dependence. The angular dependence of NEXAFS resonances in molecular adsorption systems are described in Ref.2. Figure 2 shows linear regression for the π^* resonance of aryl ring. Intensity ratios were plotted as a function of $\cos^2\theta$. The gradient of spectrum was used to obtain a tilt angle. The aryl ring of MBA SAM is estimated to 31 degree inclined from surface normal.

Then, phosphorescence spectrum of MBA SAM was measured using UV laser. Excitation wavelength was 340 nm. Figure 3 shows phosphorescence spectrum of MBA SAM measured at 77K. Phosphorescence was observed at 450-550 nm region. The lifetime of phosphorescence measured at 484 nm was 17ms. Phosphorescence spectra were also measured at 77K for MBA film and MBA ethanol solution. The lifetime of these samples were shorter than that of MBA SAM. This result shows that phosphorescence strongly depends on molecular environment.

REFERENCES

1. H. Baba and M. Kitamura, *J. Mol. Spectrosc.* **41**, 302-309 (1972).
2. J. Stöhr, NEXAFS Spectroscopy, Springer-Verlag: New York, 1992.

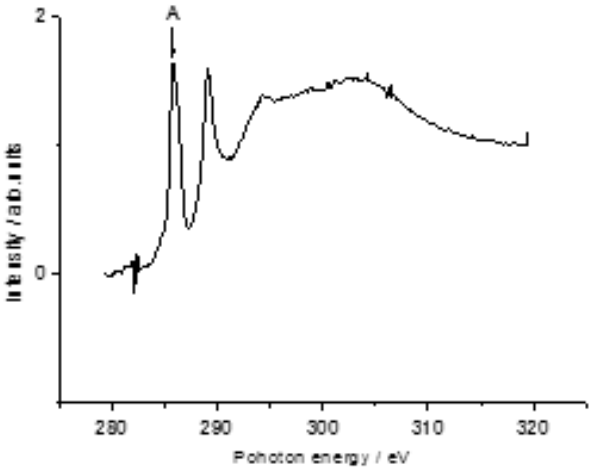

FIGURE 1. Carbon K-edge NEXAFS spectrum of MBA SAM. Incidence angle is 90 degree.

.

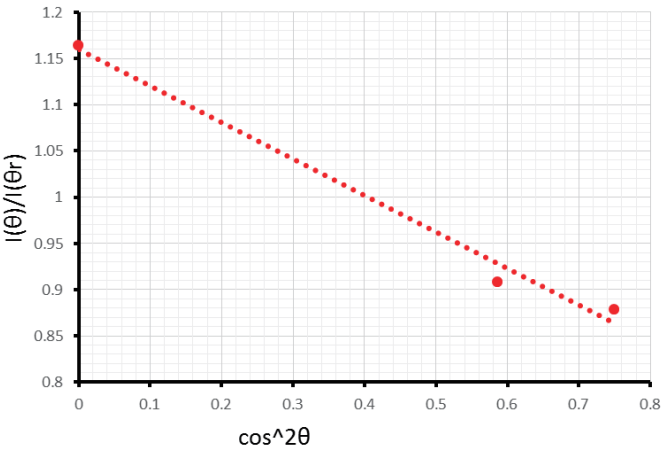

FIGURE 2. Linear regression of the aryl ring π* intensity obtained from NEXAFS spectra of MBA SAM.

.

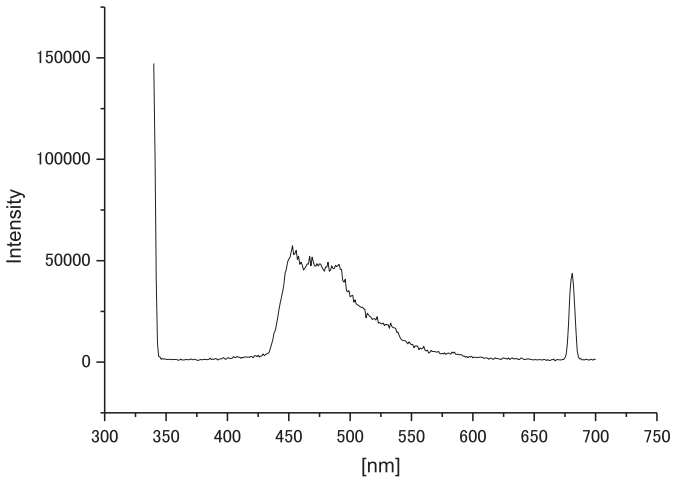

FIGURE 3. Phosphorescence spectrum of MBA SAM measured at 77K. Excitation wavelength is 340 nm.

Evaluation of Ultrathin Multilayer Films Produced by Layer-by-Layer Method Using Conventional Spraying

M. Matsue[a], S. Wada[a,b], T. Umemoto[a], and A. Hiraya[a,b]

[a] *Department of Physical Science, Hiroshima University, Higashi-Hiroshima 739-8526, Japan*
[b] *Hiroshima Synchrotron Radiation Center, Hiroshima University, Higashi-Hiroshima 739-0046, Japan*

Keywords: Layer-by-Layer method, Ultrathin multilayer films, Polyelectrolytes, Nanoparticles

Sequential deposition of nanomaterials possesses an attractive potential of developing materials, devices, and coating with new functionality. Layer-by-Layer (LbL) technique is one of prospective methods to form ultrathin multilayer films by utilizing electrostatic force [1]. In many cases, LbL films have been formed by dipping a previously charged substrate into a polycation and a polyanion solution alternately and repeatedly (Fig. 1(a)). Insertion of charged nanoparticles (NPs) can also make it possible to form well-stacked NPs (Fig. 1(b)). Such LbL procedure is quite easy but needs much dipping time to deposit enough polyelectrolytes onto a substrate.

Reentry, Schlenoff et al. reported the construction of an electrolyte multilayer film by an alternative method, spraying the respective solutions on the substrate [3]. Spraying is convenient, fast, and more generally applicable for the coating of large surfaces. In this study, we prepared conventional spray system for LbL technique by using altered commercial sprays and formed ultrathin multilayer films were evaluated by spectroscopic methods.

LbL multilayer films were formed by polycations, poly(allylamine hydrochloride) (PAH, MW ~15,000) and poly(ethylenimine) (PEI, MW ~25,000), and polyanion, poly(sodium 4-styrenesulfonate) (PSS, MW ~70,000). Molecular structures of these polymers are listed in Fig. 2. Fig. 3 shows the setup for spraying LbL technique prepared for this study. Aqueous solutions of above polyelectrolytes are alternately sprayed over Si or glass substrates.

First, multilayer films formed by polyelectrolytes on Si substrate are evaluated by X-ray photoelectron spectroscopy

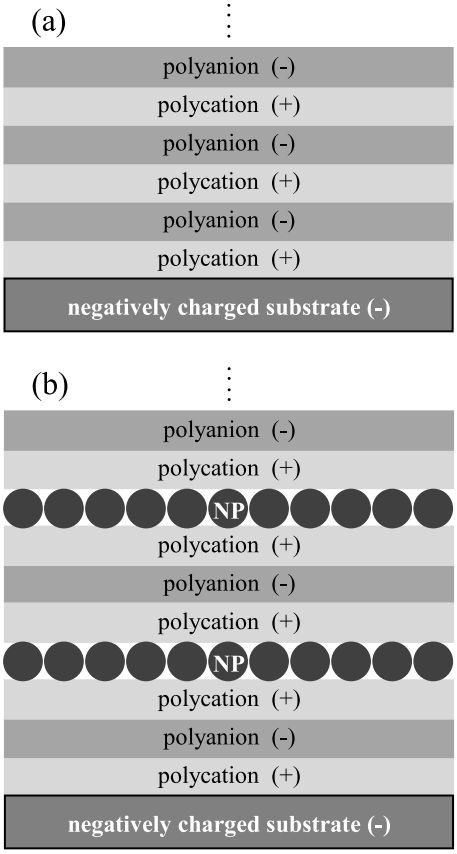

FIGURE 1. Schematic drawing of ultrathin multilayer films stacked by electrostatic force using Layer-by-Layer technique. Multilayer films are formed (a) only by polyelectrolytes and (b) by inserting nanoparticles (NPs).

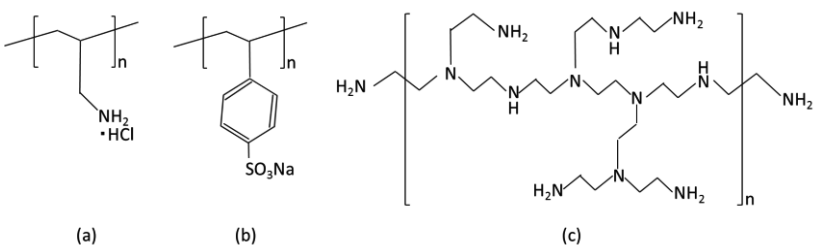

FIGURE 2. Polyelectrolytes used in this study. (a) PAH (poly-(allylamine); polycation), (b) PSS (poly(styrenesulfonate); polyanion), and (c) PEI (poly(ethylenimine); polycation).

(XPS) using synchrotron radiation at BL-13 of HiSOR. Fig. 4 shows XPS spectra around the Si 2p region measured for multilayer films with different number of spraying cycles, n=15, 20 and 30. XPS signal from a Si substrate is attenuated by increasing spraying cycles, that is number of layers. XPS intensity I can be written by attenuation length λ, number of spraying cycles n, and thickness of a pair of polycation and polyanion films d, and XPS intensity from non-deposited clean Si substrate I_0,

$$I = I_0 e^{-nd/\lambda}.$$

Using XPS intensities in n=15 and 20 and λ for electron kinetic energy of 430 eV, λ=14 Å [4], we can derive the thickness of a multilayer by one spraying cycle to be 4 Å.

Sequential deposition of nanomaterials is also evaluated using nanocrystals of poly(diacetylene) derivative (PDA, inset of Fig. 5) sprayed onto a glass substrate in the same manner as depicted in Fig. 1(b). Fig. 5(a) shows absorption spectra measured for different spraying cycles n: (PDA/polymers[+/-/+])$_n$, indicating the increase of absorption peaks at 593 and 643 nm come from PDA nanocrystals. Fig. 5(b) shows intensity plot of 643 nm peak depending on number of spraying cycles n. The plot indicates clear linear dependence, indicating the formation of quantitatively well-uniform layers of PDA nanocrystals.

References

1. G. Decher and J.B. Schlenoff Eds., *Multilayer Thin Films: Sequential Assembly of Nanocomposite Materials*, Weinheim: Wiley-VCH, 2003.
2. G. Decher, *Science* **277**, 1232-1237 (1997).
3. J.B. Schlenoff, S.T. Dubas, T. Farhat, *Langmuir* **16**, 9968-9969 (2000).
4. C.L.A. Lamont and J. Wilkes, Langmuir, **15**, 2037-2042 (1999).

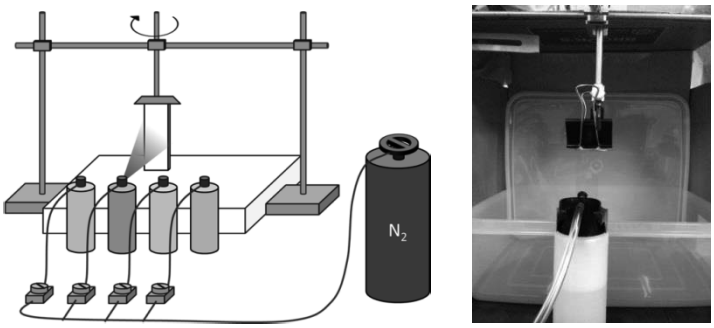

FIGURE 3. Setup for spraying LbL technique prepared for this study.

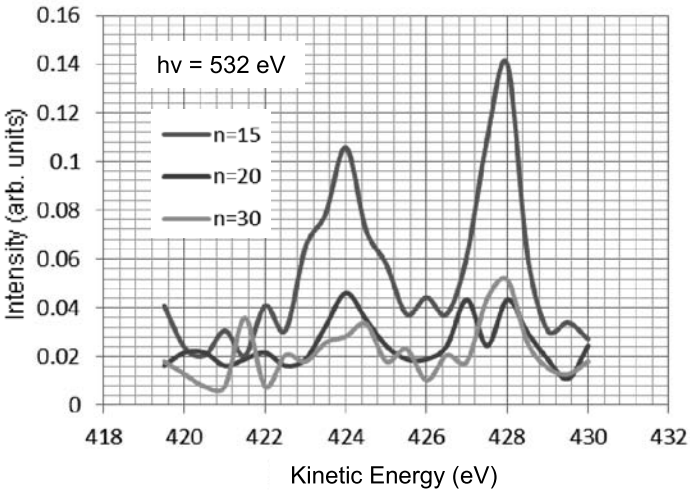

FIGURE 4. Si 2p XPS spectra measured for polyelectrolyte multilayers made by spraying cycles with 15, 20, and 30.

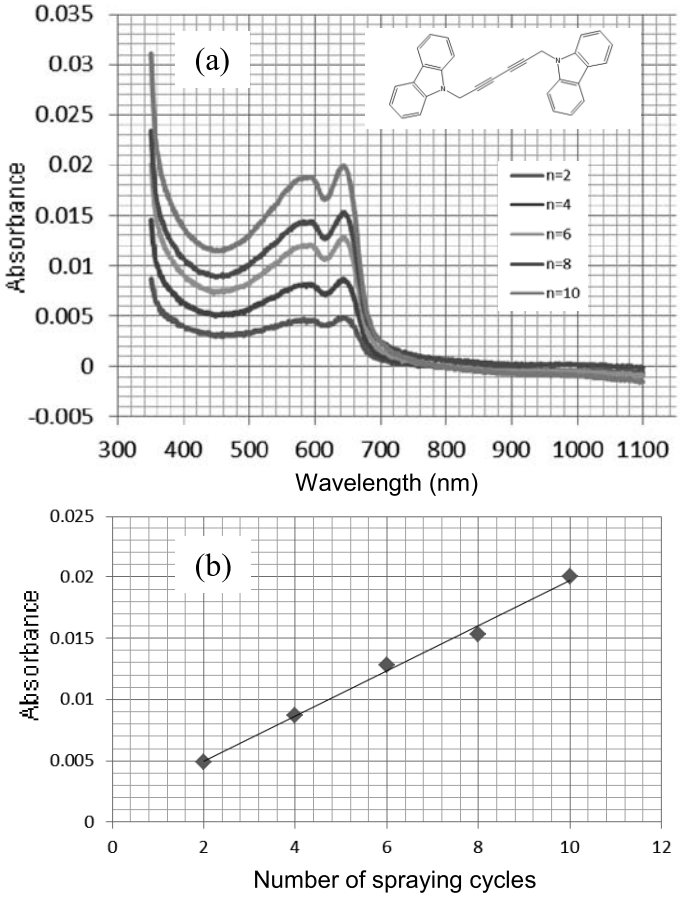

FIGURE 5. (a) Optical absorption spectra measured for multilayers of PDA nanocrystals formed by LbL technique. (b) Intensity plot of 643 nm peak depending on number of spraying cycles n, (PDA/polymers[+/-/+])$_n$.

X-ray absorption spectroscopy study of $(Na_{1-x}Ca_x)Cr_2O_4$

H. Yamaoka[a], Y. Yamamoto[b], M. Sawada[c], Y. Sakurai[d], N. Tsujii[d], K. Shimada[c], H. Namatame[c], M. Taniguchi[c,e], and J. Mizuki[b]

[a]*RIKEN SPring-8 Center, Sayo, Hyogo 679-5148, Japan*
[b]*Graduate School of Science and Technology, Kwansei Gakuin University, Sanda, Hyogo 669-1337, Japan*
[c]*Hiroshima Synchrotron Radiation Center, Hiroshima University, Higashi-Hiroshima, Hiroshima 739-0046, Japan*
[d]*Quantum Beam Center, National Institute for Materials Science, 1-2-1 Sengen, Tsukuba 305-0047, Japan*
[e]*Graduate School of Science, Hiroshima University, Higashi-Hiroshima, Hiroshima 739-0046, Japan*

Keywords: x-ray absorption spectroscopy, $NaCr_2O_4$, colossal magnetoresistance

$NaCr_2O_4$ shows an unusual CMR (colossal magnetoresistance) [1-5]. In $NaCr_2O_4$ at low temepratures the magnetoresistance increases with log-scale with decreasing temperature, while the normal magnetoresistance materials show decrease of the resistivity.

We measured the temperature dependence of the x-ray absorption spectra at O *K* and Cr $L_{2,3}$ edges. The measurements were performed with the total electron yield mode for the fractured sample surfaces. Figure 1 shows the spectra for $(Na_{1-x}Ca_x)Cr_2O_4$ (x = 0, 0.2, 0.4, 0.6, 0.8, and 1.0) measured at 60, 150, and 300 K at HiSOR BL-14. The charge state of Cr is Cr^{3+} for $CaCr_2O_4$. Chemical substitution of Ca to Na site is considered to change the Cr charge stage from $Cr^{3.5+}$ to Cr^{3+}. The O *K*-edge spectrum mainly consists of sharp peak around 529 eV (peak a), second large peak (peaks b, c, and d), and wide peak (peaks e and f). We observed x dependence for these peaks clearly. The intensities of peaks a and b decrease with x and do suddenly between x = 0.6 and 0.8. While, the intensity of peak c increases with x. The intensity of peak e also show a sudden increase between x = 0.6 and 0.8. In the Cr x-ray absorption spectra the intensity of peak k also show a sudden decrease between x = 0.6 and 0.8. On the other hand, general trend of the temperature dependence is unclear and little temperature dependence is observed.

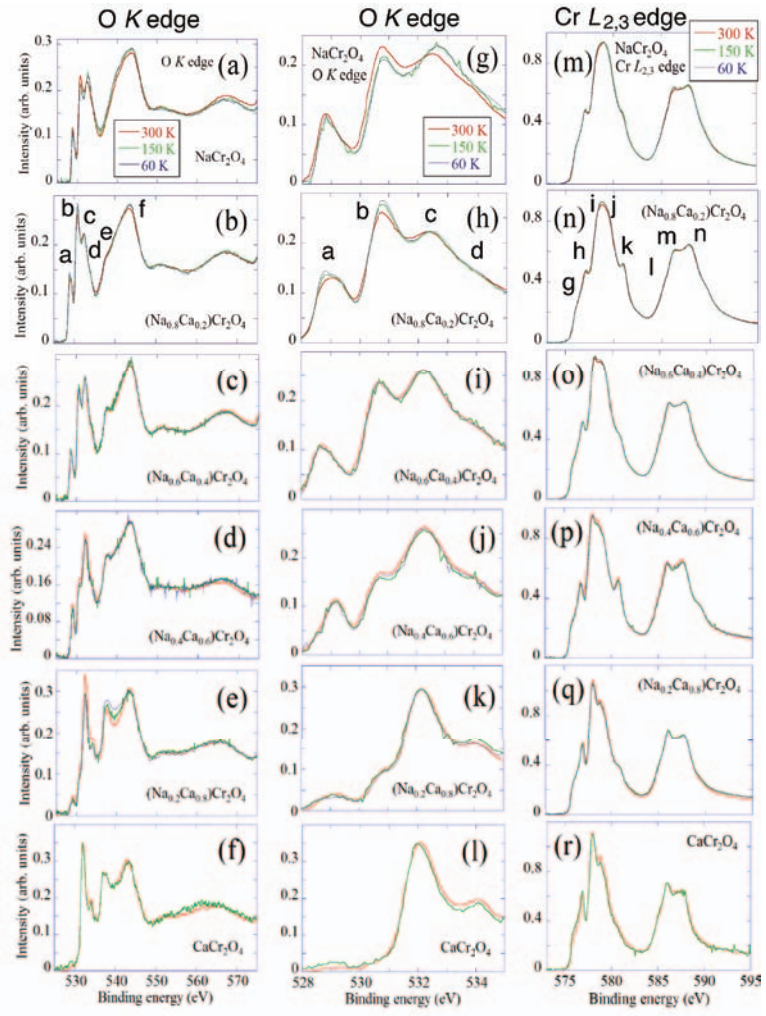

FIGURE 1. (a)-(f) X-ray absorption spectra at O *K* edge for for $(Na_{1-x}Ca_x)Cr_2O_4$ (x=0, 0.2, 0.4, 0.6, 0.8). (g)-(l) Expanded view of (a)-(f) below 535 eV. (m)-(f) X-ray absorption spectra at O Cr $L_{2,3}$ edge.

Anomalous magnetiresistance has been observed under magnetic field of around 7 T [1]. Here we study the effect of the magnetic field on the absorption spectra. Figure 2 shows the absorption spectra at O *K* edge with and without magnetic field of 1.1 T at 110 and 300 K. In these measurements clear temperature dependence is observed; the intensities of peaks a and b increase at 110 K for x = 0, and 0.15. Magnetic filed of 1.1 T also induces the increase of the intensities for the peaks a, b, and c.

We observed both effects of temperature and magnetic field on the O *K* absorption spectra. Physical meaning of the phenomena will be clarified comparing the experimental results with the theoretical calculations.

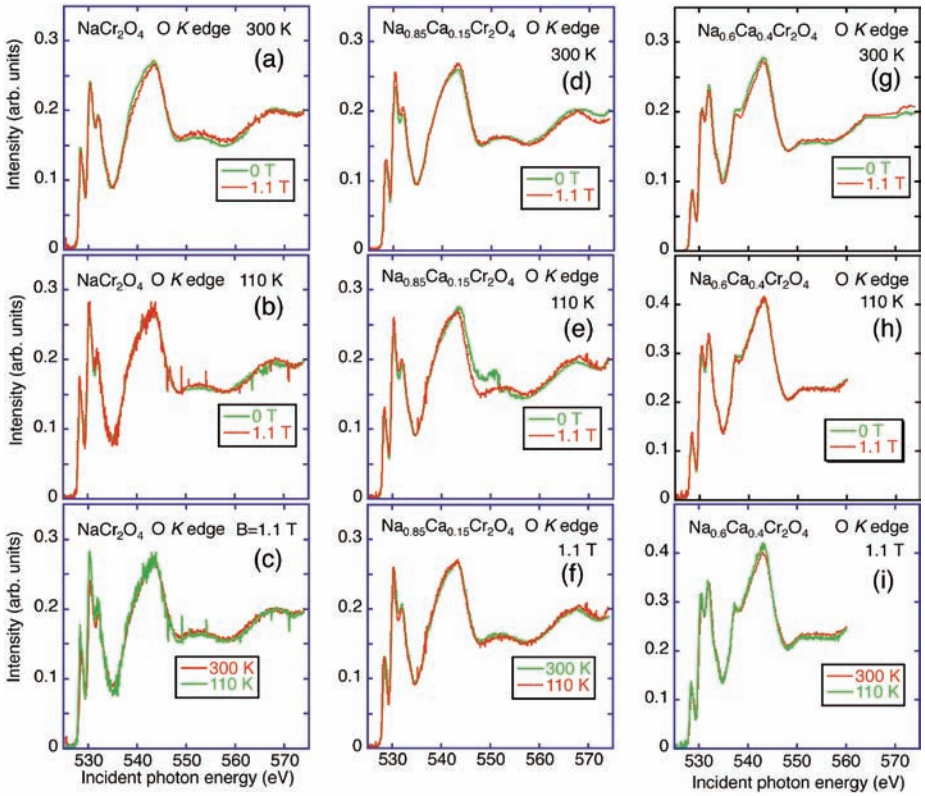

FIGURE 2. Temperature (300 and 110 K) and magnetic field (1.1 T) dependences of the x-ray absorption spectra at O *K* edge for $(Na_{1-x}Ca_x)Cr_2O_4$ (x = 0, 0.15, and 0.4).

References

1. H. Sakurai, T. Kolodiazhnyi, Y. Michiue, E. takayama-Muromachi, Y. Tanabe, and H. Kikuchi, Angew. Chem. Int. Edit. **51**, 6653 (2012).
2. H. Takeda, M. Itoh and H. Sakurai, Phys. Rev. B **86**, 174405 (2012).
3. H. Takeda, Y. Shimizu, M. Itoh, H. Sakurai, and E. Muromachi, J. Korean Phys. Soc. **62**, 1914 (2013).
4. H. Sakurai, J. Korean Phys. Soc. **63**, 583 (2013).
5. H. Sakurai, Phys. Rev. B **89**, 024416 (2014).

Magnetic Properties and Surface Structure of Graphene/Fe/Ni(111)

W. Tadano[a] , S. Matsuoka[b], M. Sawada[c], H. Namatame[b], M. Taniguchi[b,c]

[a]*Department of Physical Science, Graduate School of Science, Hiroshima University, 1-3-1 Kagamiyama, Higashi-Hiroshima, 739-8526, Japan*
[b]*Department of Physical Science, Faculty of Science, Hiroshima University, 1-3-1 Kagamiyama, Higashi-Hiroshima, 739-8526, Japan*
[c]*Hiroshima Synchrotron Radiation Center, Hiroshima University, 2-313 Kagamiyama, Higashi-Hiroshima, 739-0046, Japan*

Keywords: graphene, iron, nickel; X-ray magnetic circular dichroism, low energy electron diffraction

Graphene is one of prospective candidates for the base material for developing spintronics devices [1, 2], because ballistic electronic transport is realized in the graphene layer where spin-conserving current can be utilized if spin polarized electrons are injected effectively [3, 4]. In order to establish the spin injection technique into graphene, it is essential to clarify the magnetic properties and magnetic states at the interfaces between graphene and ferromagnetic metals. Previously magnetic states in graphene/1ML-Fe/Ni(111) system have been investigated [5]. X-ray magnetic circular dichroism (XMCD) spectra at the carbon *K*-edge have revealed an induced spin magnetic moment in the graphene layer, which is positive evidence for the spin injection. In the case of Fe intercalation of 1 and 2 ML, the Fe layers are stacked so as to keep fcc structure of the Ni(111) substrate [6]. However, relationship between magnetism and surface structure of graphene/Fe/Ni(111) system has not been revealed yet. In this study, we have investigated magnetism and surface structure of graphene/Fe/Ni(111) system, in the ultrathin film limit of Fe layers, by means of XMCD and low energy electron diffraction (LEED).

High-quality graphene can be grown on Ni(111) surface by cracking of propylene (C_3H_6) gas [7, 8]. Post-annealing procedure after an iron deposition onto graphene/Ni(111) promotes intercalation of Fe underneath the graphene layer, leading to inert effect of the Fe film which is protected by the graphene as passivation layer [8]. We fabricated graphene/Fe/Ni(111) films for the thickness dependence measurements of XMCD spectra and LEED I-V curves, where the Fe ultrathin films had wedge-type structures up to 10ML. The XMCD experiments were performed just after the sample preparations *in-situ* at HiSOR-BL14 in Hiroshima Synchrotron Radiation Center.

Figure 1 shows *M-H* curves for graphene/Fe/Ni(111) measured at room temperature, which is obtained from magnetic field dependence of the XMCD signal at Fe L_3 absorption edge. In the measurements, normal and grazing incidence geometry was applied to detect the out-of-plane and in-plane magnetization, respectively. In all the thickness range, in-plane magnetic anisotropy of the Fe film was clearly observed as well as shape magnetic anisotropy of the Ni substrate with in-plane easy axis. It has been revealed that spin magnetic moments of Fe and Ni are ferromagnetically coupled and saturated in relatively small external magnetic field.

Figure 2 shows thickness dependence of XMCD spectra for graphene/Fe/Ni(111) measured at Fe $L_{2,3}$ absorption edge. These spectra were measured at room temperature in normal incidence geometry with external magnetic field of 1.1T. The XMCD spectra have been observed for saturated magnetization, whose spectral amplitudes are normalized by X-ray absorption spectral intensities. The reduction of the saturated spin magnetic moment per Fe atomic site is revealed with the Fe thickness increased, which implies an existence of magnetically dead layer.

Figure 3 shows images of LEED for (a) graphene/Ni(111), (b) graphene/2.5ML-Fe/Ni(111), and (c) graphene/3.6ML-Fe/Ni(111) fabricated in our experiment. In the figure 3(a) and (b), sharp three-fold symmetry spots are found, coming from fcc(111) structure of the Ni substrate. The good sharpness of LEED spots are retained after the intercalation treatment, that proves high crystallinity after the formation of graphene/Fe/Ni(111). For the samples with thicker Fe, as shown in the figure 3(c), diffuse spots were found due to increase of roughness in Fe layers.

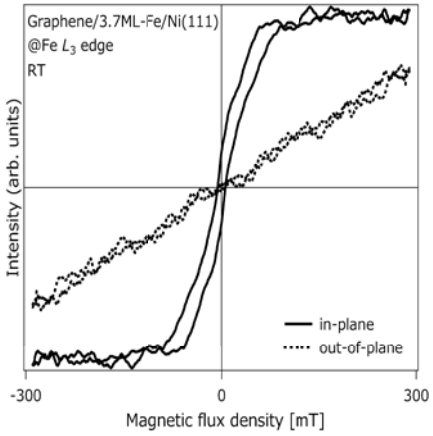

FIGURE 1. *M-H* curves for graphene/Fe/Ni(111) measured at Fe L_3 edge.

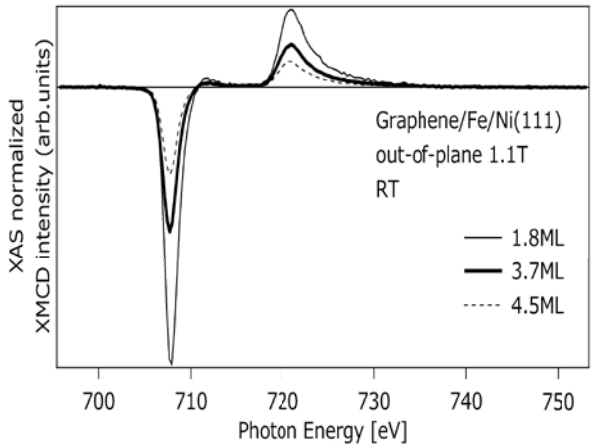

FIGURE 2. The XMCD spectra for graphene/Fe/Ni(111) measured at Fe $L_{2,3}$ edges.

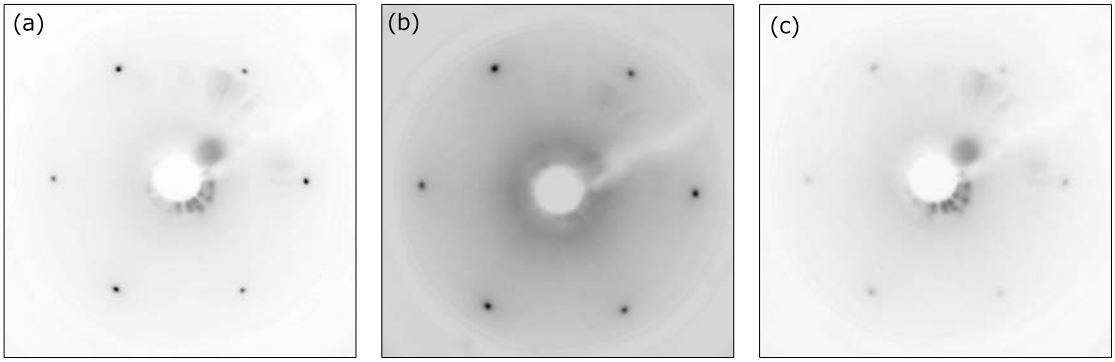

FIGURE 3. Images of LEED for (a) graphene/Ni(111), (b) graphene/2.5ML-Fe/Ni(111), (c) graphene/3.6ML-Fe/Ni(111) collected at an electron energy of 128eV.

REFERENCES

1. E. W. Hill, A. K. Geim, K. S. Novoselov, F. Schedin, and P. Blake, IEEE Trans. Magn. **42**, 2694 (2006).
2. A. K. Geim and K. S. Novoselov, Nat. Mater. **6**, 183 (2007).
3. M. Ohishi, M. Shiraishi, R. Nouchi, T. Nozaki, T. Shinjo and Y. Suzuki, Jpn. J. Appl. Phys. **46**, L605 (2007).
4. J. Maassen, W. Ji, and H. Guo, Nano Lett. **11**, 151 (2011).
5. M. Weser, E. N. Voloshina, K. Horn, and Yu. S. Dedkov, Phys. Chem. Chem. Phys. **13**, 7534 (2011).
6. E. A. Sores, G. J. P. Abreu, S. S. Carara, R. Paniago, V. E. de Carvalho, and H. Chacham, Phys. Rev. B **88**, 165410 (2013).
7. C. Oshima and A. Nagashima, J. Phys.: Condens. Matter **9**, 1 (1997).
8. Yu. S. Dedkov, M. Fonin, U.Rüdigger, and C. Laubschat, Appl. Phys. Lett. **93**, 022509 (2008).

Magnetic coupling between Mn-doped titania nanosheets and Fe overlayers

N. Saitou[a], Y. Hirano[a], M. Sawada[b], H. Namatame[b], M. Taniguchi[b], T. Taniguchi[a], Y. Matsumoto[a], M. Hara[a]

[a]*Graduate School of Science and Technology, Kumamoto University, 2-39-1 Kurokami, Kumamoto 860-8555, Japan*
[b]*Hiroshima Synchrotron Radiation Center, Hiroshima University, 2-313 Kagamiyama, Higashi-Hiroshima 739-0046, Japan*

Keywords: titania, nanosheet, XAS, XMCD, ferromagnetic, antiferromagnetic

Chemically exfoliated two-dimensional (2D) oxide nanosheets have been extensively studied in the past two decades and can be used as building blocks for future 2D devices [1,2]. Stacked multilayer films of titanium oxide (titania) nanosheets doped with 3d transition metals (Co, Fe, Mn) exhibited ferromagnetic behaviors even at room temperature [3-6]. Magnetic behaviors of the 2D magnetic semiconductors in isolated single-layer forms are not clear at the moment. In this report, we focus on single-layer Mn-doped titania nanosheets and report their magnetizations and magnetic couplings between Fe overlayers.

Mn-doped titania nanosheets ($Ti_{0.73}Mn_{0.20}O_2$) are obtained from (Li/Mn)-cosubstituted layered titanate [6]. FIGURE 1(a) shows a scanning electron microscope (SEM) image of the Mn-doped titania nanosheets deposited on a heavily doped Si substrate by a Langmuir-Blodgett (LB) technique. Nanosheets are densely covered with the surface of the Si substrate. The lateral size of the nanosheets is the order of hundreds of nanometers. An atomic force microscope (AFM) image of the nanosheets is also shown in FIG.1(b). The height of the single-layer is about 1.6 nm as shown in FIG.1(c) and is comparable to the reported value in the earlier work [6].

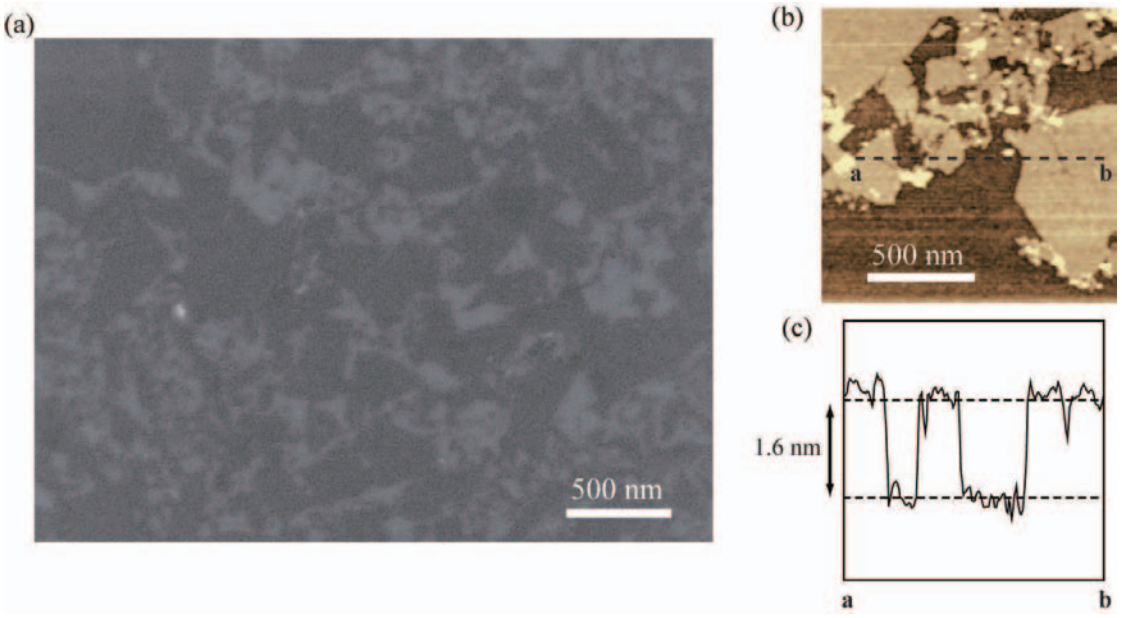

FIGURE 1. (a) SEM image of $Ti_{0.73}Mn_{0.20}O_2$ nanosheets (dark contrast) on Si substrate (bright contrast) without Fe overlayers. (b) AFM image of the nanosheets. (c) Height profile along the line shown in (b).

Soft X-ray absorption spectroscopy (XAS) and X-ray magnetic circular dichroism (XMCD) experiments were carried out at BL-14 beam line. The spectra were taken in total electron yield mode by measuring the drain current through the Si substrate. The directions of the incident X-ray and the external magnetic field of 1.1 T were perpendicular to the sample as shown in FIG.2(a). Fe overlayers were deposited on the Mn-doped titania nanosheets in the UHV chamber of the beam line for avoiding surface oxidations. The thicknesses of the Fe layers were spatially varied from 0 ML to 5.3 ML. In the measurements, the external magnetic field was switched between parallel and antiparallel to the fixed photon helicity at each photon-energy step.

The sign of the XMCD signals at absorption edges reveals the direction of spin magnetic moment to the external magnetic field. Negative (Positive) signal at L_3 edge means parallel (anti-parallel) alignment to the magnetic field. The normalized XMCD asymmetry value at the L_3 edge as a function of Fe thickness is shown in FIG.2(b). The asymmetry value depends on the Fe thickness, which indicates that the magnetizations of Fe were not fully aligned along the external perpendicular magnetic field of 1.1 T especially for thinner films. It decreases with the Fe thickness and takes a minimum value of -0.27 for the thickest 5.3 ML film, which is comparable to the reported value of a fully magnetized thick Fe film [7].

The significant XMCD signal also appeared in Mn L_3 edges, although the amplitude was much smaller than that of Fe XMCD. In the absence of Fe overlayers, the Mn XMCD shows a negative sign at the L_3 edge as shown in FIG.2(c). The finite Mn XMCD signal reveals a weak ferromagnetic order in single-layer Mn-doped titania nanosheets deposited on a Si substrate even at room temperature, which is consistent with a ferromagnetic behavior of stacked films reported by the earlier work [6]. In contrast, the existence of Fe overlayers changes the sign of Mn XMCD at the L_3 edge. Moreover, the positive signal increases with the thickness of Fe overlayers. This behavior implies that there is an antiferromagnetic coupling between the magnetizations of Fe overlayers and Mn-doped titania nanosheet. Similar antiferromagnetic couplings induced by magnetic proximity effects [8] of Fe overlayers have been observed also in other Mn-doped semiconductors $Ga_{1-x}Mn_xAs$ [9] and topological insulators $Bi_{2-x}Mn_xTe_3$ [10].

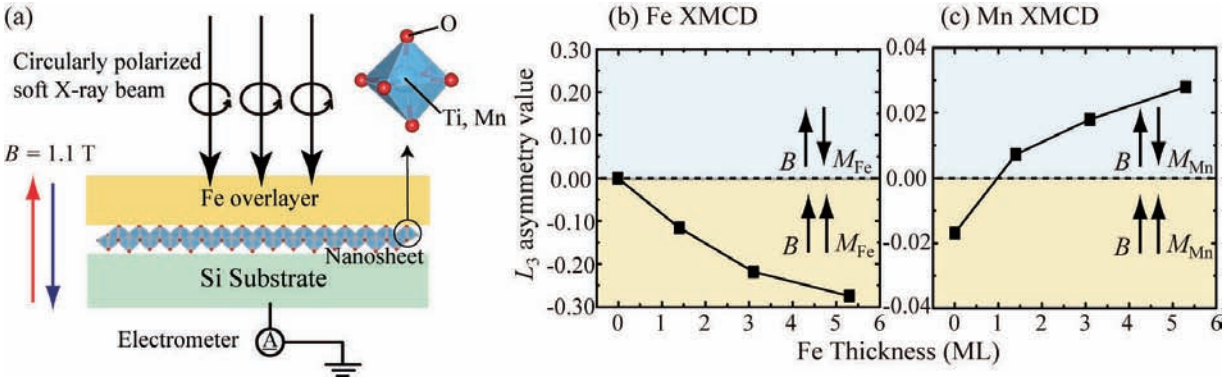

FIGURE 2. (a) Schematic illustration of the XAS/XMCD measurement setup. Crystal structure of the nanosheet is also drawn. Normalized XMCD asymmetry value at the L_3 edge for Fe (b) and Mn (c).

REFERENCES

1. R. Ma and T. Sasaki, *Adv. Mater.* **22** 5082 (2010).
2. M. Osada and T. Sasaki, *Adv. Mater.* **24** 210 (2012).
3. M. Osada et al., *Phys. Rev. B* **73** 153301 (2006).
4. M. Osada et al., *Adv. Mater.* **18** 295 (2006).
5. Y. Kotani et al., *Appl. Phys. Lett.* **93** 093112 (2008).
6. X. Dong et al., *Chem. Mater.* **21** 4366 (2009).
7. C. T. Chen et al., *Phys. Rev. Lett.* **75** 152 (1995).
8. P. K. Manna and S. M. Yusuf, *Phys. Rep.* **535** 61 (2014).
9. F. Maccherozzi et al., *Phys. Rev. Lett.* **101** 267201 (2008).
10. I. Vobornik et al., *Nano Lett.* **11** 4079 (2011).

Inverse photoemission spectroscopy of $Ca_{2-x}Sr_xRuO_4$

Yuki Utsumi[a], Stefano Agrestini[a], Liu Hao Tjeng[a],
Heisuke Nagata[b], Hitoshi Sato[b]

[a]*Max Planck Institute for Chemical Physics of Solids, Nöthnitzer Str. 40, 01187 Dresden, Germany*
[b]*Hiroshima Synchrotron Radiation Center, Hiroshima University, Higashi-Hiroshima 739-0046, Japan*

Keywords: inverse photoemission spectroscopy, metal-insulator transition

The layered perovskite $Ca_{2-x}Sr_xRuO_4$ attracts great interest due to the rich physical properties. While Sr_2RuO_4 is a paramagnetic metal and shows unconventional superconductivity below 1.5 K [1], the opposite end member Ca_2RuO_4 is an antiferromagnetic insulator below 110 K and shows a metal-insulator transition (MIT) at 357 K [2]. In the range of x<0.2, the MIT takes place at continuously decreasing temperature as the Sr content approaches the quantum critical point at x=0.2. For the case of $Ca_{1.91}Sr_{0.09}RuO_4$, the MIT temperature becomes almost equal to the magnetic transition temperature. In the $Ca_{2-x}Sr_xRuO_4$ system, the nominal electronic state of Ru is $4d^4$ (Ru^{4+}) where the 4d electrons partially occupy the t_{2g} orbitals in the low spin configuration. It has been reported that the MIT is associated with the presence of strong electron correlation effects and that it is accompanied by large changes in the t_{2g} orbital occupation [3]. Very recently, we have carried out hard x-ray photoelectron spectroscopy (HAXPES) experiments on $Ca_{1.91}Sr_{0.09}RuO_4$ and have observed dramatic changes in the valence band across the MIT. We expect to observe also large changes in the unoccupied electronic structure across the MIT.

We therefore carried out an inverse photoelectron (IPES) study on $Ca_{1.91}Sr_{0.09}RuO_4$ and a reference compound, Sr_2RuO_4. The combination of IPES and photoemission (PES) will provide us with the necessary information concerning the strength of the on-site Coulomb interaction U and will allow us to carry out a quantitative modeling of the MIT. Taking the advantage of the tunable incident electron energy, we measured also the Ru 4p-4d resonant IPES (E_K=40-50 eV) to extract the Ru 4d derived states. By comparison of the IPES spectra of Sr_2RuO_4 and $Ca_{1.91}Sr_{0.09}RuO_4$ in the metallic phase, we expected to extract quantitatively the influence of the lattice distortions on the one-electron band width.

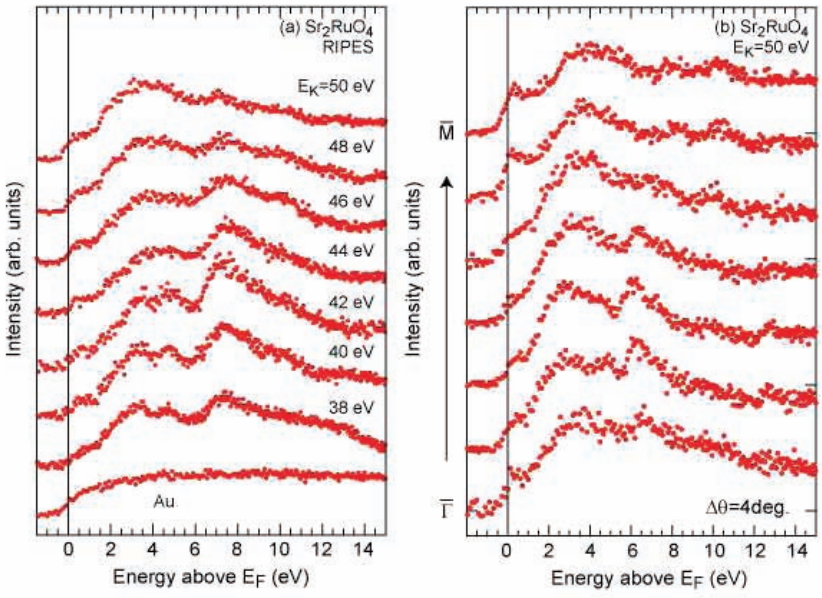

FIGURE 1. RIPES spectra of Sr_2RuO_4 (a) and angle resolved IPES spectra of Sr_2RuO_4 measured at E_K=50 keV.

Figure 1(a) shows the RIPES spectra of Sr_2RuO_4 measured at 300 K. A shoulder structure at the Fermi energy (E_F) and broad structure centered at 4 eV are assigned to the Ru t_{2g} and e_g unoccupied states, respectively. A broad peak structure around 8 eV is mainly derived from Sr 4d states. We did not observe a significant change in t_{2g} -derived structure. However, the intensity of Sr 4d states increased around E_K=42 eV.

Angle resolved IPES (ARPES) was performed along ΓM direction of Sr_2RuO_4. Fig. 1(b) shows ARIPES spectra measured by 4 degrees step at E_K=50 eV. We showed that unoccupied band dispersion of Sr_2RuO_4 can be observable by ARIPES.

Figure 2 shows the metal phase spectrum of $Ca_{1.91}Sr_{0.09}RuO_4$ measured at 200 K compared to Sr_2RuO_4. The spectral shape of $Ca_{1.91}Sr_{0.09}RuO_4$ is thoroughly different from that of Sr_2RuO_4. A peak centered at 9 eV is considered to be Ca-derived states. Unfortunately, time needed to have good statistic for the spectra was longer than expected. Therefore not enough time was left to measure with reasonable statistic the IPES spectrum of the insulating phase of $Ca_{1.91}Sr_{0.09}RuO_4$. Temperature dependence of IPES measurement should be performed again on $Ca_{1.91}Sr_{0.09}RuO_4$.

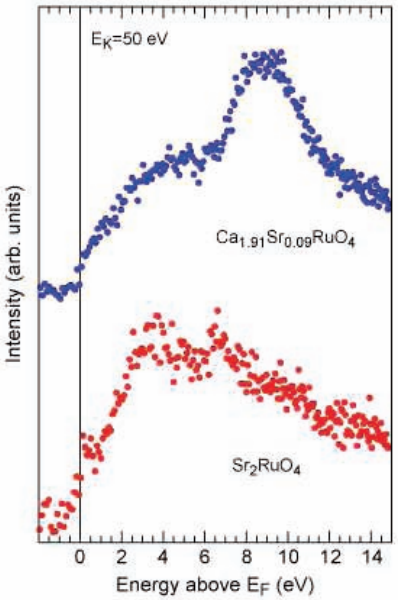

FIGURE 2. IPES spectra of $Ca_{1.91}Sr_{0.09}RuO_4$ and Sr_2RuO_4 in the metal phase measured at E_K=50 keV.

REFERENCES

1. Y. Maeno *et al*., Nature (London) 372 (1994) 532; A. P. Mackenzie *et al*., Phys. Rev. Lett 80 (1998) 161.
2. S. Nakatsuji *et al*., J. Phys. Soc. Jpn. 66 (1997) 1868; C. S. Alexander *et al*., Phys. Rev. B 60 (1999) 8422.
3. T. Mizokawa and L. H. Tjeng *et al*., Phys. Rev. Lett. 87 (2001) 77202; Phys. Rev. B 69 (2004) 132410.
4. E. Gorelov *et al*., Phys. Rev. Lett. 104 (2010) 226401.

ARPES and inverse ARPES study of strongly-correlated electron system $SrVO_3$

S. Yamamoto[a], D. Shimonaka[a], T. Yoshida[a], A. Fujimori[b],
H. Sato[c], H. Namatame[c], M. Taniguchi[c,d],
H. Kumigashira[e], K. Ono[e], S. Miyasaka[f], S. Tajima[f], and S. Biermann[g]

[a]*Graduate School of Human and Environmental Studies, Kyoto University, Kyoto 606-8501, Japan*
[b]*Department of Physics, University of Tokyo, Bunkyo-ku, Tokyo 113-0033, Japan*
[c]*Hiroshima Synchrotron Radiation Center, Hiroshima University, Higashi-Hiroshima 739-0046, Japan*
[d]*Graduate School of Science, Hiroshima University, Higashi-Hiroshima 739-8526, Japan*
[e]*Photon Factory, Institute of Materials Structure Science, KEK, Tsukuba, Ibaraki 305-0801, Japan*
[f]*Graduate School of Science, Osaka University, Osaka 560-0043, Japan*
[g]*Centre de Physique Th´eorique, Ecole Polytechnique, CNRS-UMR7644, 91128 Palaiseau, France*

Keywords: Electron correlation, Mass renormalization, ARPES, IPES

Transition-metal oxides have been studied extensively because of their interesting physical properties such as high-T_c superconductivity, colossal magnetoresistance and metal-insulator transitions, and these physical properties occur due to strong electron correlation. Among them, $SrVO_3$, which is a Pauli-paramagnetic metal with a cubic perovskite structure, has Mott-Hubbard-type electronic structure with one electron in V 3*d* orbital and its electronic structure has been studied experimentally and theoretically.

In previous angle resolved photoemission spectroscopy (ARPES) studies of $SrVO_3$, coherent part corresponding to the quasiparticle bands and incoherent part due to electron correlation were observed near E_F. Particularly, the band dispersions of the quasiparticle in the coherent part are renormalized compared with the prediction of LDA calculation, indicating mass renormalization due to electron correlation [1]. In a naive picture, one may expect that mass renormalization factor would be the same between the occupied and unoccupied bands. However, a recent GW+DMFT calculation suggested weak mass renormalization in the unoccupied state compared to that of the occupied state [2].

In this study, we have studied the occupied and unoccupied electronic structure of $SrVO_3$ by ARPES and inverse ARPES, respectively. ARPES measurements were performed at beamline 28A of Photon Factory with a Scienta SES-2002 electron analyzer. Inverse ARPES measurements were performed at HiSOR. Figure 1(a) shows the normal emission spectra of the occupied state taken by changing photon energy. On the other hand, Figure 1(b) shows the normal emission spectra of the unoccupied state taken by changing incident electron energy. We have observed the changes of the spectral line-shape near E_F in the unoccupied state at E_K = 50 - 65 eV, indicating band dispersions similar to the occupied state.

In order to see V 3*d* band dispersions more clearly, image plots in Figure 2 have been deduced by taking second derivative of the spectra in Figure 1. Compared with LDA calculation, one can find that the effective electron mass is enhanced in both sides. Moreover, the mass renormalization in the unoccupied state is smaller than that of the occupied state. While the energy of the band bottom in the occupied state is reduced to ~45% of that in LDA calculation ($m^*/m_b \sim 2.2$), the energy of the band top in the unoccupied state is ~70% of the calculation result ($m^*/m_b \sim 1.4$). The observed asymmetric mass renormalization is qualitatively consistent with the result of GW+DMFT calculation [2]. The present result provides new insight into the understanding of strongly correlated electronic structure.

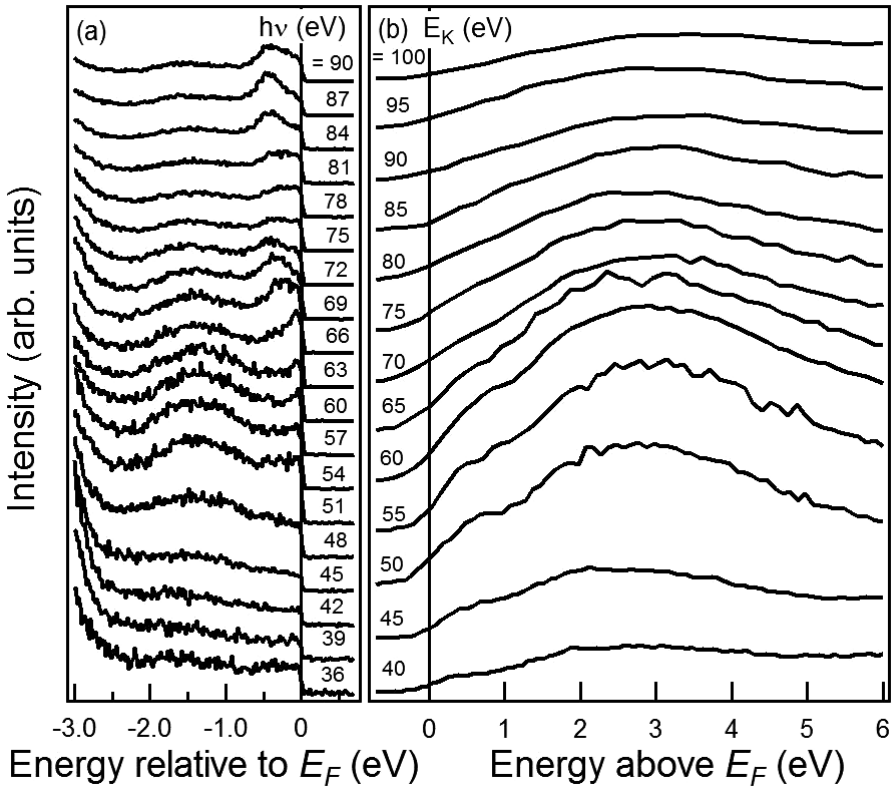

FIGURE 1. Normal emission spectra of $SrVO_3$ near E_F. (a) ARPES spectra taken at 20 K. (b) Inverse ARPES spectra taken at 300 K.

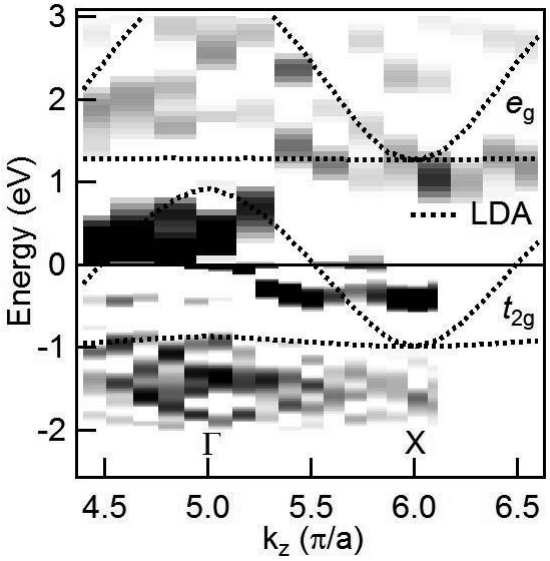

FIGURE 2. Quasiparticle dispersions of $SrVO_3$ in the occupied and unoccupied state deduced by taking second derivative of the spectra in Figure 1. Dashed lines show the result of LDA calculation. In the unoccupied state, the structure at ~1 eV around the X point is e_g band corresponding to the LDA calculation. On the other hand, the structures around 1.5 eV below E_F and 2 eV above E_F are incoherent part.

REFERENCES

1. T. Yoshida *et al*., Phys. Rev. B **82,** 085119 (2010).
2. Jan M. Tomczak, M. Casula, T. Miyake, and S. Biermann, Phys. Rev. B **90,** 165138 (2014).